Iron-rich microband formation in marine sediments by hydrothermal iron cycling bacteria at Lucky Strike

Jérémie Aubineau, Ernest Chi Fru, Christine Destrigneville, Thierry Decrausaz, Fleurice Parat, Fabien Baron, Alexandra Nederbragt, Manuel Henry, Alain Castillo, Céline Rommevaux, et al.

To cite this version:

Jérémie Aubineau, Ernest Chi Fru, Christine Destrigneville, Thierry Decrausaz, Fleurice Parat, et al.. Iron-rich microband formation in marine sediments by hydrothermal iron cycling bacteria at Lucky Strike. Communications Earth & Environment, 2025, ⟨10.1038/s43247-025-02223-2⟩. ⟨hal-05053696⟩

HAL Id: hal-05053696
https://hal.science/hal-05053696v1

Submitted on 2 May 2025

communications earth & environment

A Nature Portfolio journal

Article

https://doi.org/10.1038/s43247-025-02223-2

Iron-rich microband formation in marine sediments by hydrothermal iron cycling bacteria at Lucky Strike

Jérémie Aubineau[1] ✉, **Ernest Chi Fru**[2], **Christine Destrigneville**[1], **Thierry Decrausaz**[3], **Fleurice Parat**[3], **Fabien Baron**[4], **Alexandra Nederbragt**[2], **Manuel Henry**[1,5], **Alain Castillo**[1], **Céline Rommevaux**[6] & **Valérie Chavagnac**[1]

Models describing banded iron formation deposition beneath oxygenated Paleoproterozoic marine shelf waters assume that microaerophilic iron-oxidizing microorganisms were significant contributors. However, direct evidence for this mechanism is lacking, and it remains unclear how associated primary organic biomass and biogenic iron oxyhydroxides transformed into organic carbon-poor iron oxide/carbonate-rich bands in banded iron formations. Here we explore in situ modern Zetaproteobacterial iron-oxidizing mats thriving in the Lucky Strike hydrothermal vent field to develop an empirical model that explains the potential contribution of iron-based metabolisms to deposition of rocks resembling banded iron formations. Petrographic, mineralogical, and geochemical data suggest that abundant production of Zetaproteobacterial stalks nucleates and drives spontaneous biotic/abiotic ferrihydrite precipitation in the mats. Subsequent early diagenetic anaerobic microbial oxidation of dead biomass as the mats aged, coupled to microbial reduction of iron oxyhydroxides/oxides, generates ferrous carbonates and mixed valence magnetite. Collectively, this forms crystalline iron-rich organic carbon-lean ^{13}C-depleted layers reminiscent of Precambrian banded iron formation microbands.

Banded Iron Formations (BIFs) are ancient marine chemical sedimentary deposits rich in iron (Fe) and silica (Si), with peak deposition 4000–1850 Million years (Ma) ago and briefly during the 720–635 Ma Neoproterozoic Snowball Earth glaciations[1–3]. They provide key information about the chemistry of the ancient seawater from which they were formed and about the iron cycling in the early oceans. Algoma-type BIFs, often interlayered with Archean-Paleoproterozoic-aged volcano-sedimentary sequences, are interpreted to have been deposited near submarine volcanic centres via exhalative-hydrothermal processes[1,2]. Their distinct sedimentary and geochemical features suggest an open or partially restricted deep sea depositional setting. Algoma-type BIFs tend to be widespread in Archean cratons and sporadically appear in Proterozoic marine sedimentary environments. The deposition of Quaternary Algoma-type BIF analogue rocks on the coast of Milos, Greece[4,5] suggests Algoma-type BIFs may also be associated with near continental margin shallow hydrothermal vent fields, driven by microbial iron cycling[6,7]. In contrast, Superior-type BIFs are typically interbedded with Paleoproterozoic carbonates and black shales, reflecting deposition in nearshore shelf environments[1,2]. Algoma-type BIFs are much thinner and smaller in lateral extent than Superior-type BIFs, although the former can be more abundant in individual occurrences[8]. Rapitan-type BIFs, linked to the Neoproterozoic Snowball Earth glaciations, were formed when thick ice sheets resulted in the deoxygenation of the seawater, enabling ferruginous conditions to develop in the global ocean through hydrothermal exhalation[2].

Generally, BIFs contain at least 15 wt.% bulk Fe and often show spectacular alternating millimetric (microbands) to metric silica and Fe(III) oxide or Fe(II) silicate layers[1–3]. According to a consensual model, the large-scale accumulation of Fe required that dissolved Fe(II) sourced from hydrothermal vents was oxidized by various mechanisms to insoluble Fe(III) in association with abiotic precipitation of amorphous silica[1]. Existing geochemical models propose that the microbands in Algoma-type BIFs likely formed through seasonal variations or microbial activity[9]. Similar

---

[1]Géosciences Environnement Toulouse, CNRS UMR 5563 (CNRS/UPS/IRD/CNES), Université de Toulouse, Observatoire Midi-Pyrénées, Toulouse, France. [2]Center of Geobiology and Geochemistry, School of Earth and Environmental Sciences, College of Physical Sciences and Engineering, Cardiff University, Cardiff, Wales, UK. [3]Géosciences Montpellier, Université de Montpellier, CNRS, Montpellier, France. [4]Université de Poitiers, IC2MP CNRS, Poitiers, France. [5]CEFREM, Université de Perpignan Via Domitia, UMR 5110, CEDEX, 52 Avenue Paul Alduy, Perpignan, France. [6]Aix-Marseille University, Université de Toulon, CNRS, IRD, MIO, Marseille, France. ✉e-mail: jeremaubineau@aol.com

microbial mechanisms have been suggested for the deposition of Quaternary shallow submarine hydrothermal vent field analogues[4,5]. However, there is a notable lack of in situ studies that detail the pathways of Fe(II) oxidation leading to the formation of primary amorphous Fe(III) minerals in BIFs and the processes involved in the sequential transformation of these minerals into highly crystalline Fe(III) phases with low organic carbon content, remain understudied. Here, we provide a mechanism from a modern environment that could support a potential biological origin for Algoma-type BIF-like microbands in a modern deep-sea hydrothermal setting.

Planktonic (i) O_2-producing photosynthetic cyanobacteria in the Proterozoic Ocean, coupled with abiotic Fe oxidation, or chemolithoautotrophic Fe(II)-oxidizers, and (ii) Archean anoxygenic photoautotrophic Fe(II)-oxidizing bacteria (photoferrotrophy)[6,10–13], are among some of the most prominent mechanisms proposed for Precambrian BIF deposition. For example, microaerophilic Fe(II)-oxidizing microorganisms (FeOM), including *Zetaproteobacteria*, that likely evolved to dominate pelagic microaerobic conditions following the Great Oxidation Event (GOE), ca. 2500–2100 Ga[14,15], are suggested to have produced a “ferrihydrite rain” to the Precambrian seafloor[2]. In contrast, a consortium of benthic microbial communities may have formed discrete microbands of iron oxides in stromatolitic facies[16]. However, it remains unclear how these processes and benthic microbial communities contributed to the generation of BIF bands.

Although present in varying amounts, iron oxides in Archean and Proterozoic BIFs are dominated by magnetite ($Fe(III)_2Fe(II)O_4$) and haematite ($Fe(III)_2O_3$), respectively[17]. Both are interpreted as having formed from an initial poorly crystalline Fe(III)-oxyhydroxide precursor phase, such as ferrihydrite[1,3] (Fh – $Fe(III)(OH)_3$), suggesting the iron oxide mineralogy of Precambrian BIFs is likely secondary rather than primary. Alternatively, greenalite ($Fe(II)_3Si_2O_5(OH)_4$) formed under oxidant-depleted environmental conditions, has been suggested as an alternate primary Fe precursor in BIFs[18–20] prior to the GOE. Based on this theory, iron oxides in Archean BIFs are secondary products formed following post-depositional oxidation of the primary ferrous silicates[21,22]. In addition, green rust, a ferrous–ferric hydroxy salt, which would have precipitated near the Fe redoxcline and transformed into stable mineral phases (e.g., magnetite) within the water column and sediments, has been suggested as a precursor to BIF mineral assemblages[23]. Consequently, there is no consensus on the dominant Fe mineral precursors to BIFs. One reason for these disagreements arises from the scarcity of modern analogues of banded Fe-Si-rich precipitates from diverse marine settings mimicking the Precambrian Ocean to enable the appropriate testing and validation of these various hypotheses.

Moreover, the low organic matter content of BIFs has been used to dismiss the potential direct involvement of biological activity in the precipitation of BIF Fe(III)-rich minerals. However, near-complete respiration/oxidation of organic matter coupled to Fe(III) reduction by various bacteria and archaea are frequently hypothesized to explain the low organic C content (<0.8 wt.%) in BIFs[1,12,24]. This view is anchored on intimately associated magnetite and ^{13}C-depleted Fe(II)-bearing carbonates (e.g., siderite), and the general absence of definitive microfossils preserved in the non-silicified Fe-rich bands[1,24]. However, direct (i.e., textural) evidence for biological activity provided by microfossils and stromatolitic oncoidal structures associated with granular IF deposition has been recently documented[25–27]. Therefore, understanding the complex interplay between BIFs, ocean chemistry, and the biosphere to unravel the mechanisms responsible for the extensive generation of organic C-lean BIFs, remains an ongoing endeavour as are the pathways involved in the transformation of primary Fe-bearing mineral precursors into crystalline phases.

To provide new insights into these primary and secondary BIF formation pathways, we focus on present-day active submarine hydrothermal ecosystems displaying high dissolved Fe fluxes associated with chemolithoautotrophic microaerophilic FeOMs, typical of the mid-ocean ridges, back-arc spreading centres, and submarine arc volcanoes[28]. There, hydrothermal fluid discharge produces chemical and redox gradients that enable the development of a variety of microbial mats along cracks and fractures on various seafloor lithologies[29–35]. Although deep-sea hydrothermal environments have been widely studied for their microbial composition and environmental conditions, there is a dearth of knowledge on their potential association with the biological development of Precambrian BIFs[35–39]. We therefore collected in situ modern Fe-rich microbial mats from the Lucky Strike Hydrothermal Field (LSHF; 37°17’N & 32°16’W; Mid-Atlantic Ridge[40]) (Fig. 1; Table 1; Supplementary note 1), to investigate a potential linkage and association. At the seafloor, white and orange microbial mats, linked to sulphur oxidation[30] and Fe oxidation[29,41], respectively, flourish on a heterogeneous substratum in close vicinity of diffuse vents at temperatures <100 °C[42,43] from different well-known sites, including Capelinhos (CAP), North Tour Eiffel (NTE), South Isabel (SI), West Sintra (WS), and Y3.

Given the relatively high Fe(II) concentrations in Archean oceans (μM then versus nM today)[44], it is commonly accepted that deep-marine hydrothermal vents in the Archean delivered tremendous amounts of Fe(II) and other reduced compounds that modulated nutrient cycling (e.g., C, N, S, Fe) and contributed to BIF deposition[1,45]. The LSHF mats host abundant microbial communities, including autotrophic Fe(II)-oxidizing *Zetaproteobacteria* coexisting with N, S, and methane-cycling microorganisms[29,41] (see Supplementary note 1). *Zetaproteobacteria* are the presumed primary producers in iron-rich mats flourishing in diverse hydrothermal environments[41,46] as they are obligate chemoautotrophs, oxidizing Fe(II) to gain energy. Thus, they are essential for the development of ecological niches within the mats produced in Fe(II)-rich hydrothermal vent fields.

Considering that metabolic pathways within such nutrient cycles (i.e., C, N, S, Fe) emerged and diversified in the Archean[45], including microaerophilic microbial Fe oxidation[47], we couple petrographic and mineralogical observations with C-N systematics in the LSFH mats to validate primary and secondary microbial processes potentially involved in BIF microbands. We discuss the possibility that similar mat-forming FeOMs could have contributed to the generation of microbands in BIFs that formed close to hydrothermal vent field settings, for example, Algoma-type BIFs, under constrained microaerobic environmental depositional conditions and hydrothermal exhalation of Fe(II)-rich fluids.

Results

Texture and mineralogy of microbial mats

Except for the Lava Lake (LL) site where no diffuse venting was observed, two types of microbial mats, dominated by crumbly and flocculent structures, flourished in the vicinity of diffuse hydrothermal fluid venting at CAP, NTE, SI, WS, and Y3 (Fig. 1)[48–50]. Coherent and porous deposits with variable thickness of <20 cm, together with occasional dark-coloured laminated structures typify the crumby microbial mats located at the CAP, NTE, and Y3 sites (Figs. 1, 2a−i, 3a−g, and 4a−i; Table 1). The mats at the SI, WS, and LL sites are composed of a mixture of flocculent material associated with microorganisms and inorganic particles (Fig. 1; Table 1). All the sampled Fe-rich mats have been previously studied for their Zetaproteobacterial diversity and microbial filament morphology[29].

Based on petrographic observations, the CAP mats dominantly exhibit mm-scale outward-convex structures with internal concentric bands consisting of a more or less porous network of filamentous structures dominated by stalks (Fig. 2b−h), a typical feature linked to FeOMs[51]. The twisted stalks, among other morphologies of filaments in the CAP mats[29], are thought to reflect dynamic microbial mat growth features[13,52]. X-ray diffraction (XRD) patterns further show two broad peaks centred at ~2.70–2.90 Å and ~1.51 Å (Fig. 5; Supplementary Fig. 1), which deviate from the pure 2-line Fh peaks characterized by d-spacings at 2.54 and 1.47 Å[53,54]. This shift, together with the poorly resolved peak at ~1.51 Å, the energy-dispersive spectra (EDS) analysis (Fig. 2i), and infrared-based spectroscopy (Supplementary Figs. 2, 3 & Supplementary note 2), point to poorly crystalline Si-bearing Fh[55,56]. The combined datasets highlight that the Fe-rich microstructures are heavily mineralized by Si-bound Fh.

Contrary to the CAP site, mat growth patterns are not visible at the NTE site. Instead, micronodule structures of <120 μm in diameter and angular minerals from the altered substratum compose the mats (Fig. 3b–f). Results from XRD, Mössbauer and infrared-based spectroscopies, and EDS analyses highlight the widespread occurrence of poorly crystalline Mn oxides (todorokite, birnessite, and pyrolusite), anorthite, and amphibole (edenite), and Si-bound Fh as the main Fe(III)-rich mineral (Figs. 3g, 5; Supplementary Figs. 1—3; Supplementary Table 1).

The Y3 mats comprise two Fe-rich microbands composed of multiple laminated and upward-convex layers (Fig. 4a, b), probably reflecting successive steps of mat growth[52]. Petrographic observation of the bottom most part of the mats is distinctively represented by a mm-thick black band consisting mainly of siderite and magnetite that appear as isotropic octahedral crystals showing a higher reflectance relative to other Fe(III)-rich minerals (iron oxides and well-crystallized Fe(III)-oxyhydroxides are referred to as FeOx) (Figs. 4c—e, 5; Supplementary Fig. 1). Towards the top of the mats, the black laminae are succeeded by alternating dark and light brown laminated layers composed of well-crystallized FeOx of various crystal shapes, including goethite [α-Fe(III)OOH], lepidocrocite [γ-Fe(III)OOH], and akageneite [β-Fe(III)OOH·Cl] (Figs. 4f—h, 5; Supplementary Figs. 1—3 & Supplementary note 2). In contrast to the other LSHF mats, little Si is bound to these FeOx in all laminae as suggested by the lack of an EDS Si peak, high EDS Fe/Si ratios, and the absence of Fe-O-Si stretching (Fig. 4i; Supplementary Figs. 3, 4). In addition, Mössbauer spectroscopy was employed to confirm the presence of Fh in the Y3 mats (Fig. 5; Supplementary Table 1 & Supplementary note 2). Similar to CAP mats and other natural biofilms[57], microbial filaments predominantly composed of stalks, coral-like, and Y-shaped structures at Y3 associated with *Zetaproteobacteria*[29], are thickly coated with poorly crystalline Fh. From top to bottom, the Y3 mats contain Fh-encrusted microbial filaments that disappear at the expense of increasing enrichment of well-crystallized FeOx minerals and ferrous carbonates (Fig. 6).

The Fe mineralogy of the flocculent mats at the WS, LL, and SI sites is dominated by both Si-Fh and Fh phases (Fig. 5; Supplementary Figs. 2, 3; Supplementary Table 1). Neither Si-rich bands nor amorphous silica phases like opal-A, common in modern marine sediments and defined by a broad peak centred at ~4.10 Å (~25.2° 2θ CoKα)[31,32,34,58,59] were evidenced by XRD and petrographic observations in the LSFH mats. Finally, unidentified organic molecules are associated with the Fh-dominated mats (Supplementary Fig. 3).

Bulk geochemistry

Bulk mat geochemistry at LSHF shows heterogeneous chemical major element composition, with Fe_2O_3 content varying between 10.8 and 99.6 % (Supplementary Table 2 & Supplementary note 2). At the NTE site, elevated concentrations of Al_2O_3 and CaO ranging from 9.4–13.3 % and 4.2–6.2 %, respectively, compared to other sites with <3.3% Al_2O_3 and <1.6% CaO, are related to basaltic-derived alteration fraction composed of anorthite and amphibole. P concentrations vary considerably in function of Fh/FeOx mineralogy, where very low (<0.04 %) P content is associated with crystalline FeOx phases and high (0.15-0.72 %) P concentrations with poorly crystalline Fh (Supplementary Fig. 5), reflecting a 3- to 18-fold decrease from crystalline FeOx to poorly crystalline Fh.

X-ray fluorescence (XRF) analysis of the LSHF mats reveals SiO_2 concentrations in the range of 3.9-38.1% (Supplementary Table 3), the lowest in the Y3 mats, moderate in the CAP, WS, and LL mats, and highest in the SI and NTE mats. XRF findings agree with the above mineralogical and petrographic results and support the potential occurrence of opal-A at the SI site. Moreover, the observations indicate a limited presence of Si-bound FeOx minerals at Y3, the presence of silicate minerals at NTE, and the general lack of amorphous silica phases at LSHF.

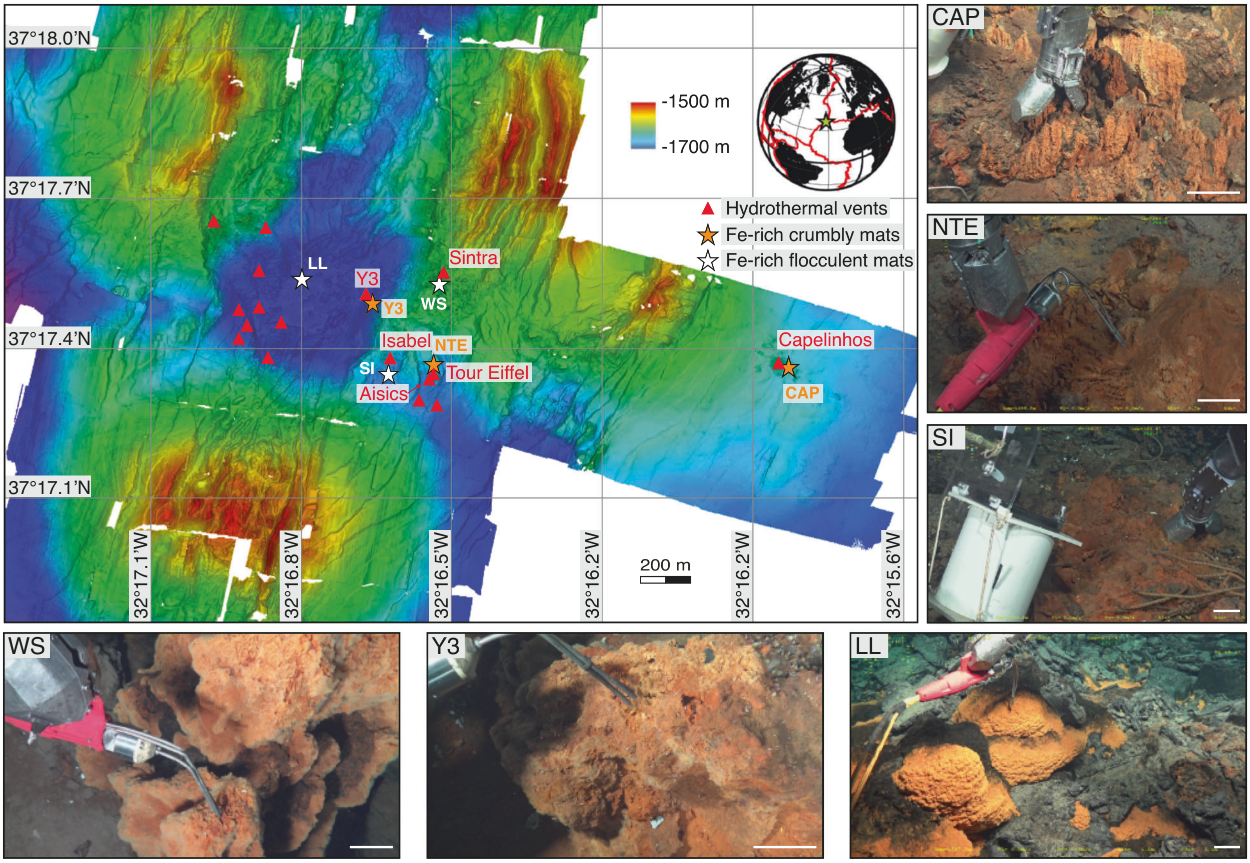

Fig. 1 | Bathymetric map of the Lucky Strike hydrothermal field and images of the sampled iron-rich microbial mats, modified from Chavagnac et al.[60] and Astorch-Cardona et al.[29]. The studied mats and their associated active hydrothermal vents are shown. No hydrothermal vent was detected at LL site. Chlorinity increases from CAP to LL sites. Scale bars: 5 cm. [Capelinhos (CAP); North Tour Eiffel (NTE); South Isabel (SI); West Sintra (WS); Lava Lake (LL)].

Table 1 | Specific features of the studied Fe(II)-oxidizing microbial mats from Lucky Strike Hydrothermal Field. For further details, see Supplementary discussion concerning the high positive $\delta^{13}C_{carb}$ values

Site	Year	Dive	Depth (mbsl)	Distance from diffuse hydrothermal vent (m)	Thickness (cm)	Mat type	Colours	Abundance of *Zetaproteobacteria* (%)†	Mineralogy of the mat	Substratum
South Isabel	2021	1998-10	1699	No diffuse flow	-	Flocculent	orange-dark brown	28.68	Ferrihydrite, barite, opal-A?	Hydrothermal slab#
N37° 17.336 W32° 16.628										
West Sintra	2021	1997-9	1669	No diffuse flow	-	Flocculent	reddish brown	44.95	Si-ferrihydrite, ferrihydrite	Massive hydrothermal deposits dominated by pyrite and marcassite
N37° 17.500 W32° 16.570										
Lava Lake	2021	2000-12	1741	No vent	-	Flocculent	orange-yellowish brown	33.21	Si-ferrihydrite	Basalt
N37° 17.549 W32° 16.790	2023	844-6	1738							
Capelinhos	2022	2035-8	1669	Immediately below	20	Crumbly	orange-yellowish brown to reddish brown	21.55	Si-ferrihydrite	Hydrothermal slab#
N37° 17.360 W32° 15.829	2023	844-6	1669							
North Tour Eiffel	2022	2033-6	1689	<1	<10	Crumbly	orange-yellowish brown, brown, and black	25.07	Si-ferrihydrite, Mn oxides, anorthite, amphibole	Hydrothermal slab# composed of sphalerite, marcassite, and barite
N37° 17.353 W32° 16.535										
Y3	2022	2034-7	1727	<1	10-15	Crumbly	light brown to orange-brown	11.69	Ferrihydrite, goethite, lepidocrocite, akaganeite, magnetite, siderite, sulphurs	Hydrothermal gravitional deposits; aggregates of iron sulfide minerals and barite
N37° 17.518 W32° 16.663	2023	846-8	1727							

All data with the exception of thickness and colours of the mats are from Matabos & Sarrazin[48]; Sarradin & Matabos[49]; Matabos[50]. The mineralogy of the LSHF mats is based on our integrated study (petrographic, XRD, and Mössbauer analyses). Salts are not included.
†, Zetaproteobacterial relative abundance within the microbial mats[29]; #, layered silicified volcaniclastic deposits; mbsl, metres below sea level.

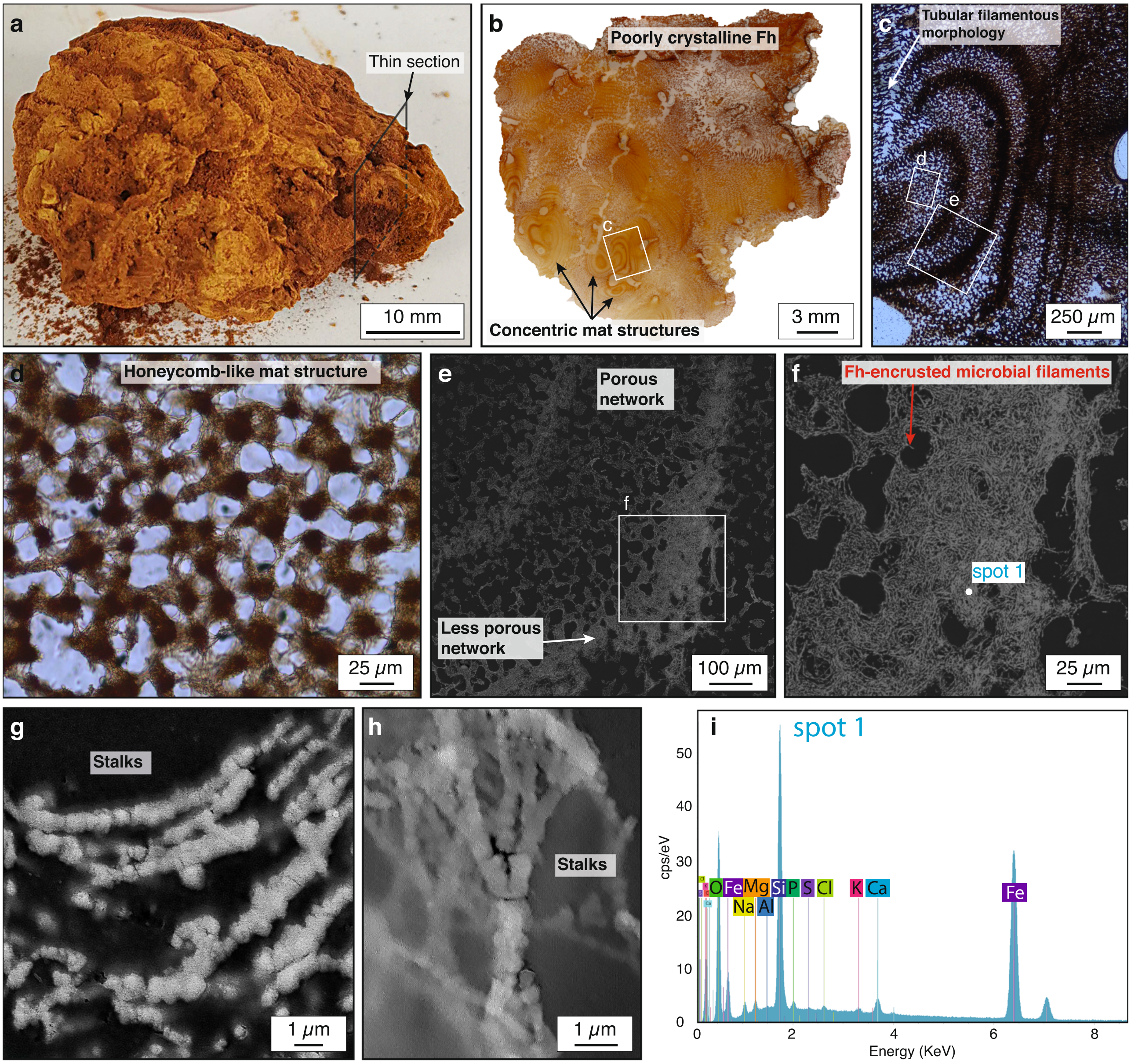

Fig. 2 | Morphological, textural, and elemental image of Capelinhos (CAP A) mat. a Brown to orange Fe(II)-oxidizing microbial mats. **b** Thin section. The Fe mineralogy exclusively consists of ferrihydrite (Fh), as demonstrated by XRD results of our study. **c, d** Transmitted light photomicrographs (plane-polarized light). Filamentous microbial structures. **e–h** SEM images in BSE mode showing the aggregation of a large number of filaments (mainly stalks here). Filaments crossing with each other to form a mesh structure. **i** EDS analysis of stalks displaying a predominantly Fe- and Si-rich composition.

Spatial chemical concentration of Fe-bearing mineral phases

Electron microprobe analyses (EPMA) align with the XRD mineralogy (Supplementary Table 4 & Supplementary note 2). Moreover, EPMA chemical compositions of Fh-encrusted filamentous microstructures and crystalline FeOx show three distinct groups in the crumbly mats (Supplementary Table 5). Considering the Si concentrations of end-member hydrothermal fluids are of the same range of concentration (12.7 to 18 mM) at LSHF[41,60], Fh in CAP and NTE sites show an average Fe_2O_3/SiO_2 ratio of 3.5 ± 1.2 ($n = 16$; 1σ), and 6.7–7.2 ($n = 2$) in the filaments of the Y3 mats, whereas a considerably higher ratio of 90.6 ± 46.6 ($n = 17$; 1σ) is recorded in the crystalline FeOx phases at Y3. The latter observation clearly aligns with electron distribution maps and infrared-based spectroscopy, illustrating stalks enriched with Si-Fh phases in the CAP mats containing quantitatively higher SiO_2 content and to a lesser extent P_2O_5 compared to the filamentous microfossils and the more crystalline FeOx minerals in Y3 mats (Fig. 7).

Carbon and nitrogen systematics

The C isotopic compositions of carbonates ($\delta^{13}C_{carb}$) and organic matter ($\delta^{13}C_{org}$) and N isotope ($\delta^{15}N$) values in the LSHF Fe-rich mats differ considerably between and within sites and samples (Table 2). These mats contain low 0.18-0.83 wt.% total organic C (TOC) and 0.02-0.07 wt.% total N (Table 2). $\delta^{13}C_{carb}$, $\delta^{13}C_{org}$, and $\delta^{15}N$ values vary from -6.0 to +11.5‰ ($n = 11$), -35.1 to -18.9‰ ($n = 11$), and -1.4 to +3.1‰ ($n = 4$), respectively. The siderite-bearing Y3 mats show negative to slightly positive $\delta^{13}C_{carb}$ values, while siderite-free mats (SI, LL, and CAP) display both negative and highly positive $\delta^{13}C_{carb}$ values. Besides, TOC contents, $\delta^{13}C_{carb}$, $\delta^{13}C_{org}$, and $\delta^{15}N$ values decrease from top to bottom with increasing siderite abundance in the Y3 B mat (Table 2). Finally, P is moderately correlated with TOC ($R^2 = 0.50$, n = 6, $p < 0.12$) (Supplementary Fig. 6a), whereas a weak covariation between $\delta^{13}C_{org}$ and $\delta^{13}C_{carb}$ ($R^2 = 0.26$, $n = 11$, $p < 0.109$) and a strong one between $\delta^{13}C_{org}$ and $\delta^{15}N$ ($R^2 = 0.74$, $n = 5$, $p < 0.054$) are observed (Supplementary Fig. 6b, c).

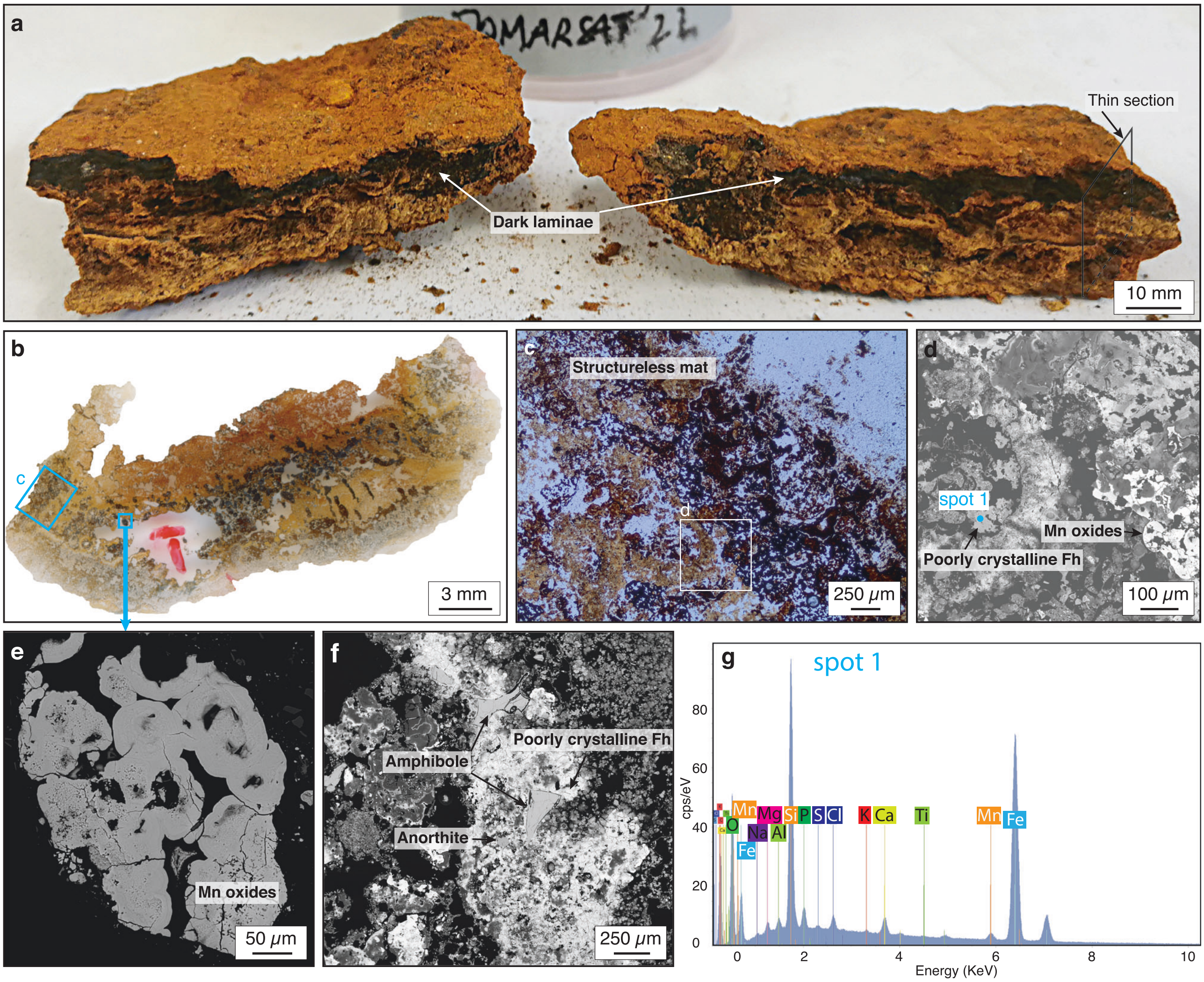

Fig. 3 | Morphological, textural, and elemental image of NTE (NTE B) mat. **a** Brown to yellowish Fe(II)-oxidizing microbial mats with mm-thick dark laminae. The sample is extremely crumbly. **b** Thin section. Note the absence of specific structures. **c** Transmitted light photomicrograph (plane-polarized light). **d–f** SEM images in BSE mode showing the presence of numerous minerals of various shapes and sizes. The Fe mineralogy exclusively consists of ferrihydrite (Fh), as suggested by the Mössbauer spectroscopy. The identification of Mn oxides and silicates was carried out with EPMA. **g** EDS analysis of Fh displaying an Fe- and Si-rich composition.

Discussion

Microbial activity

Carbon fixation and oxidation: Microaerophilic Fe(II)-oxidizing *Zetaproteobacteria*, grow at low O_2 concentrations (5–20 μM[61]) where they compete with abiotic oxidation of Fe(II) due to the slower oxidation rate in such conditions[62,63]. They use the Calvin–Benson–Bassham (CBB) pathway to autotrophically build biomass[64] according to the equation[65]:

$$6Fe^{2+} + 0.5O_2 + CO_2 + 16H_2O \rightarrow [CH_2O] + 6Fe(OH)_3 + 12H^+$$

The variable $\delta^{13}C_{org}$ values of -35.1 to -18.9‰ in the LSHF mats likely point to multiple autotrophic C fixation pathways[66,67], and potential respiration of generated organic matter by Fe(III)-reducing bacteria within the mats (Fig. 8a), connecting the Fe cycle with carbon and nitrogen cycling (see Supplementary discussion). In this regard, most of our $\delta^{13}C_{org}$ values are consistent with C fixation through the CBB cycle pathway that fractionates C_{org} isotopes by 20 to 30‰[66], considering a $\delta^{13}C$ value of the dissolved inorganic C close to 0‰. In support of this observation, the Lōʻihi seamount mats in the Pacific Ocean, containing the RubisCO gene (key enzyme in the CBB cycle)[64] and *Zetaproteobacteria*, have shown $\delta^{13}C_{org}$ values ranging from -28 to -23‰[68], which further strengthens the suggestion that *Zetaproteobacteria* contributed significantly to the $\delta^{13}C_{org}$ values bracketing between -20 and -30‰ in our samples and that they are foundational to the mat building process. In contrast, the reductive citric acid and 3-hydroxypropionate C fixing cycles produce $\delta^{13}C_{org}$ values > -20‰[66]. Except for one sample, our $\delta^{13}C_{org}$ values < -20‰ suggest that the latter autotrophic mechanisms are not dominant in the LSHF mats. Further, the anaerobic C fixation via the reductive acetyl-coenzyme A or Wood–Ljungdahl pathways produces $\delta^{13}C_{org}$ values <-30‰[46,66], similar to those observed in some Y3 mats. Although the extent of methanotrophic microorganisms is limited in the LSHF mats[29,41], they could have also contributed to the lowest $\delta^{13}C_{org}$ values due to the ^{13}C-depleted methane hydrothermal source[69] and large isotopic fractionation of up ~30‰ during methanotrophy[70].

Mechanism of microbial Fh precipitation. *Zetaproteobacteria* oxidize Fe(II) on mat surfaces, leading to even greater O_2 depletion resulting in the development of anaerobic heterotrophic microbial communities deeper in the mats. This is consistent with increasing oxidation of organic C by dissimilatory Fe(III)-reducing bacteria, resulting in a much lower residual biomass content and formation of siderite and magnetite deeper in the Y3 mat, together with more negative $\delta^{13}C_{org}$ and $\delta^{13}C_{carb}$ values[71] (Fig. 8a).

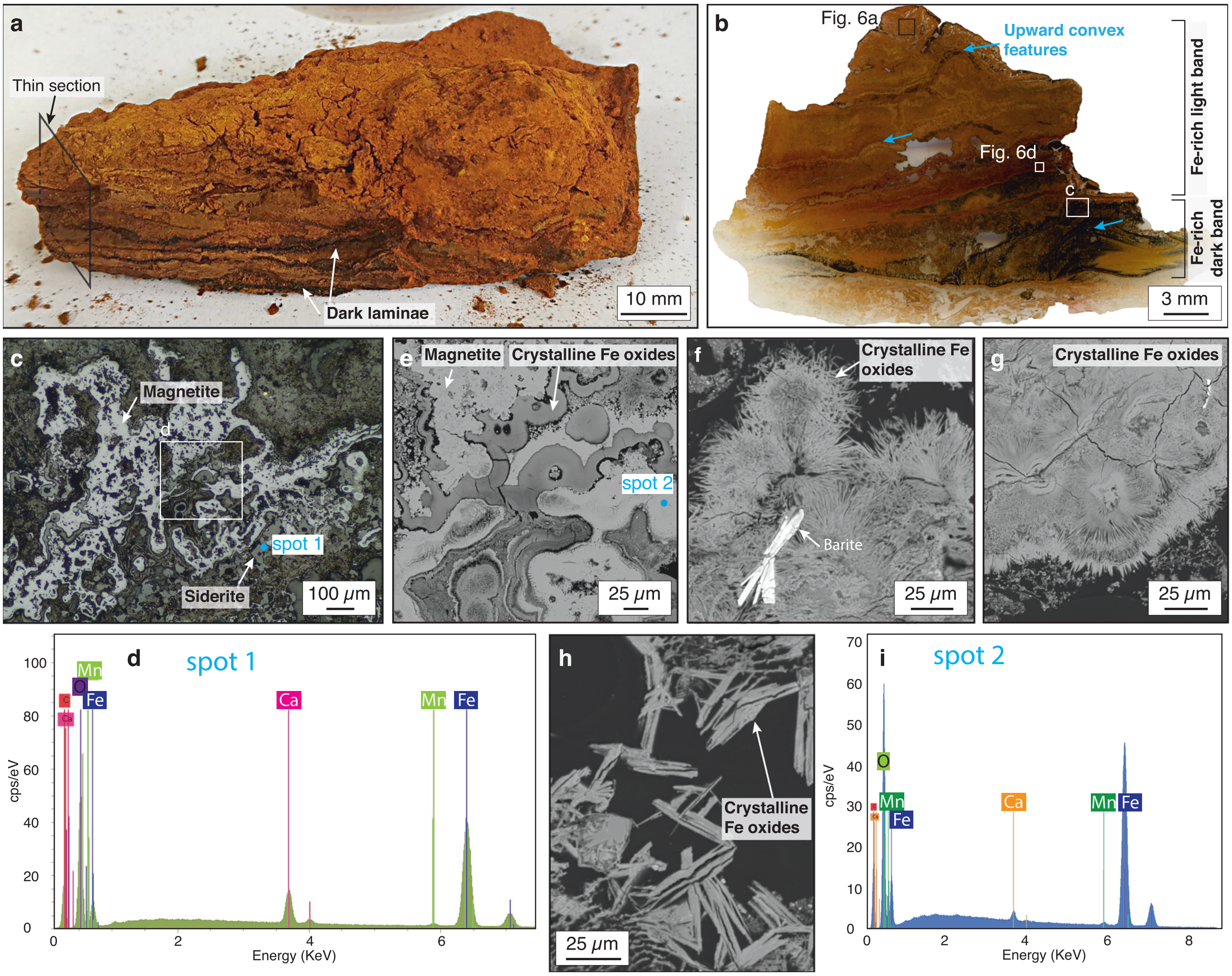

Fig. 4 | Morphological, textural, and elemental image of Y3 (Y3 B) mat. a Brown to orange Fe(II)-oxidizing microbial mats with darker bands (arrows). **b** Thin section. Note the micrometric laminated structures with darker layers towards the bottom of the mat. **c, d** Reflected light photomicrograph (plane-polarized light) of the dark layers and related EDS analysis. Close association of magnetite, a grey-coloured mineral with a higher reflectance than other Fe(III)-rich minerals, and siderite. **e–i** SEM images in BSE mode and related EDS analysis showing crystal shapes of crystalline Fe oxides and oxyhydroxides (here referred to as Fe oxides for simplicity). Highly aggregated octahedral crystals in (**e**) colloform texture with radiating fibrous morphologies in (**f**) and (**g**) and lath-like crystals in (**h**). Crystalline Fe(III)-bearing minerals mainly consist of goethite and lepidocrocite in (**f–h**), as suggested by EPMA.

Based on mineralogical and textural observations, the ubiquitous occurrence of Fh, together with abundant biogenic filaments in the studied mats, indicate initiation of poorly crystalline Fh precipitation by *Zetaproteobacteria*, with the filaments acting as nucleation sites[72]. Moreover, the stalk-/sheath-forming *Zetaproterobacteria* have been specifically linked with the LSHF mats[29], similar to many Fe-Si microbial deposits reported near modern hydrothermal vents[31,32,34,58,59,73], which are believed to reflect a response to changing Fe(II) and O_2 redox gradients[52]. Besides, the widespread association of filamentous morphologies in the LSHF mats has been suggested to represent a growth strategy that enables *Zetaproteobacteria* to escape permanent entombment and asphyxiation by Fh/FeOx precipitates[29,52]. Consequently, the resulting encrustation of abandoned filaments by Fh leads to exquisite preservation of mat growth patterns (except for the NTE site where substratum alteration occurs in this area[43]). Moreover, nucleated Fh triggers additional autocatalytic oxidation of Fe(II) in the absence of biomass, further templating and scavenging abiotic Fh from seawater[3,74].

Sequential deposition of iron oxyhydroxide phases

Fh reactivity and environmental conditions. Because of their high specific surface area and sorption capacity, poorly crystalline nm-size Fe(III)-oxyhydroxide (Fh) particles are highly reactive compared to other crystalline FeOx (e.g., goethite and magnetite)[53]. However, surface coating of Fh by organic molecules, silicate, phosphate, and trace metals may slow down or inhibit transformation into crystalline FeOx[3,54,74,75], thereby enhancing its preservation[54,76]. In this regard, our data show an abundance of organic molecules (infrared-based analyses; Supplementary Fig. 3), SiO_2, and P_2O_5 in Fh-dominated mats compared to the crystalline FeOx phases in the Y3 mats. In agreement with the accepted consensus that dissolved aqueous Si favours direct adsorption to Fh even at extremely low Si concentrations[55,77], the indurated Fh-encrusted microbial filaments at LSHF host high Si concentrations sourced from active hydrothermal vents. Further, our mineralogical observations indicate that Si tends to associate intimately with poorly crystalline Fh rather than form separate Fh and Si minerals at the surface of the mats. Similar to Si-Fh mineral associations reported in other deep-sea hydrothermal vent settings[e.g.,34], environmental factors such as fluid temperature and pH likely influenced the binding capacity of Fh for Si and various elements[78]. For example, an increase in Fh crystallite size lowers the proportion of atoms present at the mineral surface, resulting in a proportionate reduction in the mineral's specific surface area available for adsorption and/or scavenging of dissolved trace elements[54,79]. No

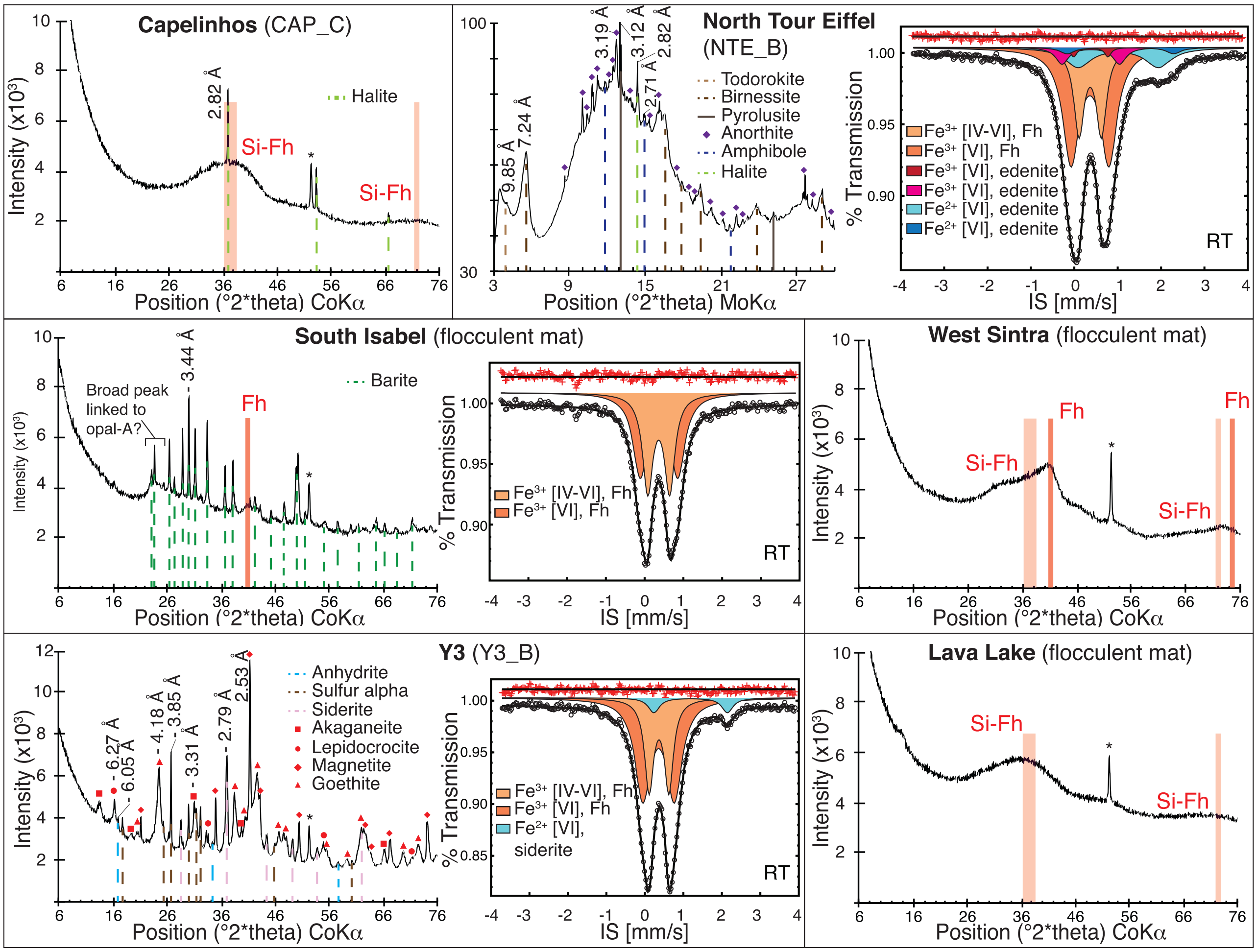

Fig. 5 | Representative XRD patterns of randomly oriented powders and Mössbauer spectra from the LSHF iron-rich microbial mats. Diagnostic XRD spacings (Å) are shown. Although the presence of crystalline minerals makes amorphous to poorly crystalline phases difficult to detect using XRD, the isomer shift (IS) and quadrupole splitting (QS) are consistent with reported values for Fh at SI, NTE, and Y3 sites (see Supplementary Note 2). The light and dark red shaded regions indicate the center of broad peak areas of Si-Fh and Fh, respectively. Note that a diffractometer using MoKα radiation was used to analyse Fe- and Mn-containing mats at the NTE site. [Ferrihydrite (Fh); room temperature (RT); diffraction peak assigned to the sample holder (*)].

correlations were observed between the pH of the diffuse hydrothermal fluids and Fh/FeOx mineralogy at LSHF (pH ranges from 5.1 to 6.1 at CAP and 5.6 to 5.8 at Y3)[42]. In contrast, persistent 90 °C diffuse fluids at Y3 compared to temperatures of ~50 °C at the CAP and NTE sites[42] would have promoted nucleation of slightly larger Fh particles at the former[78] (Fig. 8b). This phenomenon likely decreased Fh surface area reactivity, adsorption capacity for Si, P, and other elements, and likely enhanced transformation to secondary FeOx mineral phases solely in the Y3 mats.

Transformation of primary Fh to secondary Fe(III) and Fe(II) mineral phases. Different environmental conditions (e.g., temperature of diffuse fluids) at LSHF would be expected to produce different Fh transformation products. For example at the Y3 site, stalk-forming *Zetaproteobacteria* and organic molecules facilitate the nucleation of biogenic Fh[57]. As the mats aged, thermodynamically unstable Fh eventually transformed into more crystalline FeOx phases associated with residual filamentous microbial structures, as evidenced by petrographic textures (Fig. 6). Haematite formation from Fh occurs rapidly at temperatures >50 °C or after extended reaction times[80], while goethite/lepidocrocite is an intermediate mineral formed as a function of temperature, pH, and Fe(II) concentrations during the transformation of Fh to haematite[74,80]. As a consequence, the LSHF elevated Fe(II) concentrations[41,60] would have preferentially transformed Si-free Fh into goethite and lepidocrocite[3,74] (Fig. 8b), which explains the lack of haematite. This is supported by the fact that goethite may require several years/centuries (or even more) to form haematite under suitable environmental conditions, as observed in Quaternary shallow marine hydrothermal deposits associated with microbial filaments[4–6].

We observe a unique transformation of Fh/FeOx to siderite and magnetite in the bottommost part of the Y3 mat, which could result from both biotic and abiotic processes[3]. Siderite and magnetite do not appear to have replaced or overgrown an earlier Fe-rich phase. Magnetite could have formed from the conversion of Fe(III)-oxyhydroxides with the addition of high amounts of hydrothermally derived Fe(II)[74]. However, petrographic observations and all isotopic evidence suggest that they are a product of early diagenetic Fh/FeOx transformation rather than primary growth (Fig. 8b). We use C isotope systematics to decipher the origin of both minerals[24], considering the variable $\delta^{13}C_{carb}$ values could have originated from dissolved inorganic C in hydrothermal-seawater fluid mixtures because $\delta^{13}C$ values of hydrothermal vent fluids are systematically < −1‰[69]. However, the lack of correlation between Eu/Eu* anomaly as a tracer of hydrothermal contribution[81,82] and $\delta^{13}C_{carb}$ values ($R^2 = 0.03$, $n = 6$, $p < 0.75$) (Supplementary Fig. 7; Supplementary Table 2) indicates that alternative mechanisms controlled the $\delta^{13}C_{carb}$ values in the mats. Furthermore, hydrothermal fluid influence cannot explain the unique presence of siderite in the bottom layer of the Y3 mats, seeing that our samples covered several sites associated with hydrothermal activity (except for the LL site).

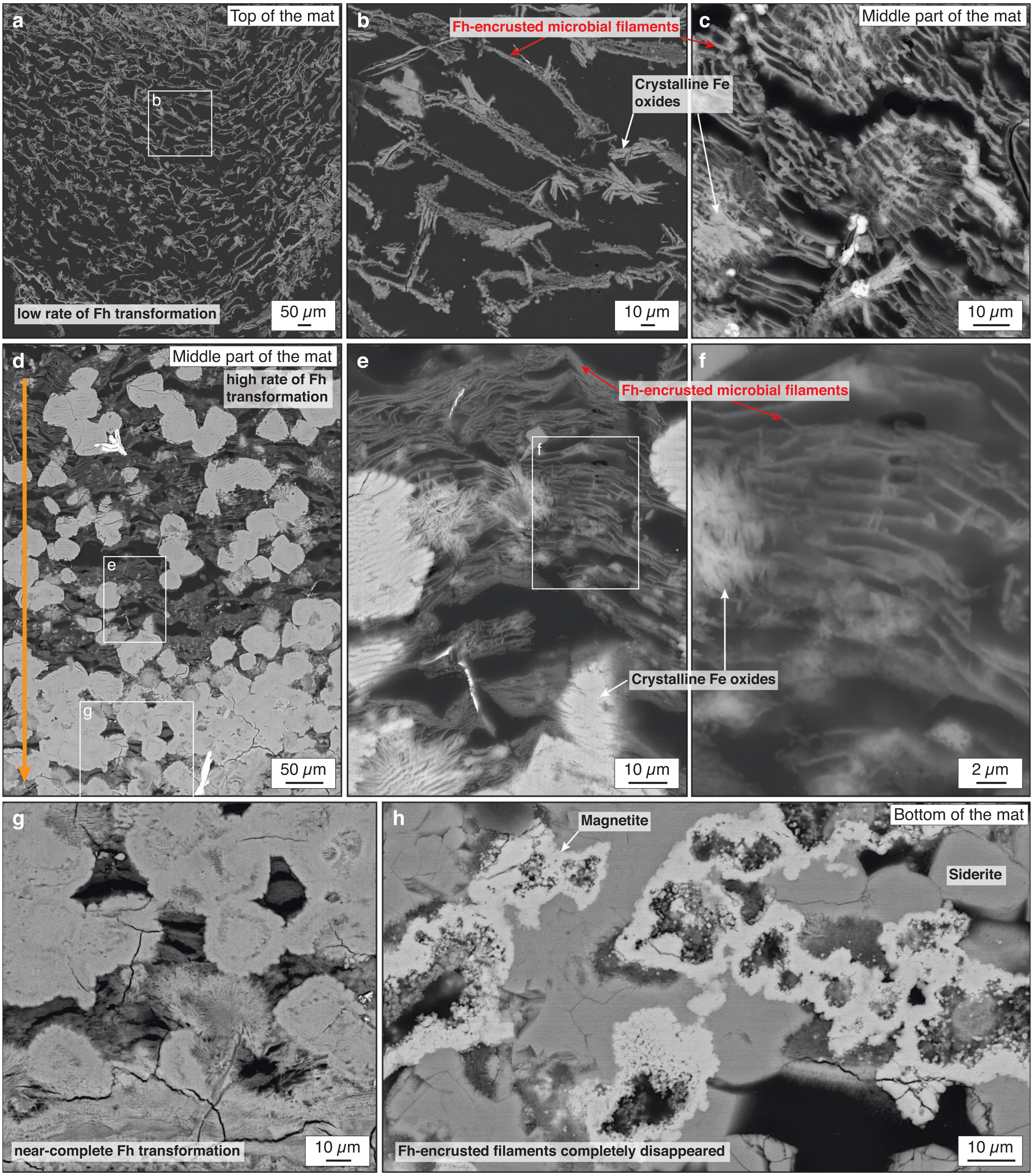

Fig. 6 | Microtextures of Y3 (Y3 B) mat. SEM-BSE images of microbial filaments showing an in situ model of increasing enrichment and crystallization of sheaths and stalks with FeOx from the upper (**a**, **b**), middle (**c**–**g**), to the bottom (**h**), parts of the Y3 B mat. As the mat aged, the microbial filaments are usually encrusted by poorly crystalline ferrihydrite (Fh)[57] first act as nucleation sites, followed by gradual transformation into well-crystallized FeOx that cover them with successive steps of FeOx crystallization (**b**–**f**), and eventually disappear (**g**–**h**). The orange arrow reported in (**d**) shows the decreasing proportion of filamentous structures with increasing depth.

Instead, the transition to lower $\delta^{13}C_{carb}$, with $\delta^{13}C_{org}$ depletion and decreasing TOC content deeper in the Y3 mat (Supplementary Fig. 6b; Table 2), as shown by the low $\delta^{13}C_{carb}$ and $\delta^{13}C_{org}$ values of +2.0‰ and -21.4‰ in the bottom part, respectively, compared to +11.5‰ and -19.0‰ at the mat surface, respectively, point to a biotic origin[71] (Fig. 8). This largely supports a coupling of early diagenetic microbial reduction of Fh/FeOx to the oxidation of residual organic C[1,12,24] to produce ^{13}C-depleted biomass and siderite, and double valence magnetite. This process is also consistent with the 3- to 18-fold reduction of P concentration in the FeOx-rich layer compared to the Fh-rich mats via the reductive release of organic-bound P into seawater and sediment pore water to sustain local primary productivity. Furthermore, the weak correlation between $\delta^{13}C_{carb}$ and $\delta^{13}C_{org}$ values in the LSHF mats implies that biologically mediated organic C oxidation promoted the release of CO_2 into pore waters, during which some combined

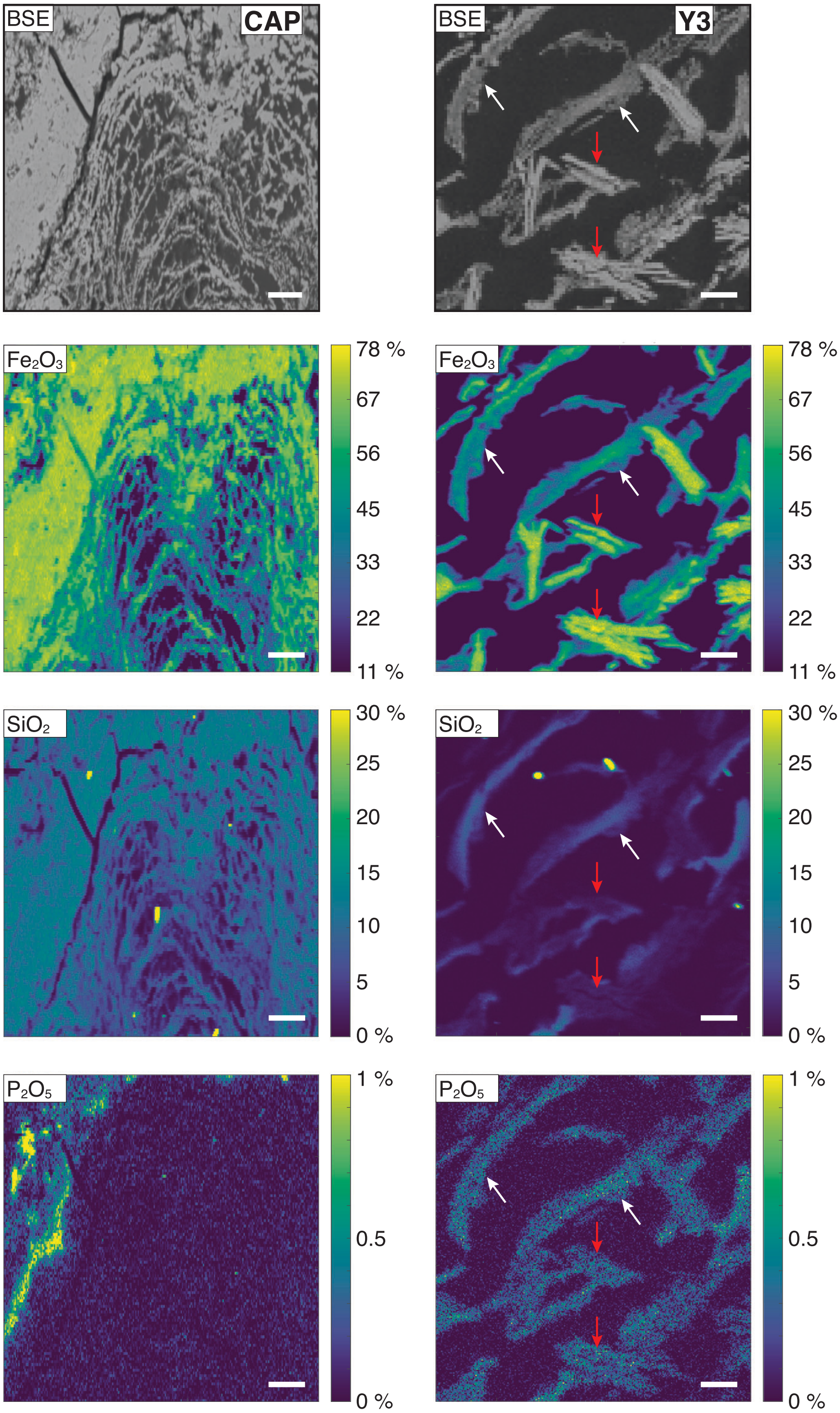

Fig. 7 | SEM-BSE images showing features of the Fe(II)-oxidizing mats from CAP (CAP A; left panels) and Y3 (top of the Y3 B mat; right panels) sites, and corresponding EPMA element mapping (viridis colour map). Fe_2O_3, SiO_2, and P_2O_5 compositional variations revealed by EMPA maps. SiO_2 and P_2O_5 concentrations in Fh-dominated CAP mat show higher proportions than those in crystalline FeOx from the Y3 mat. Red arrows denote Si-poor lath-like minerals, likely goethite/lepidocrocite, compared to Fh-encrusted microbial filaments (white arrows). Scale bars are 30 μm.

with Fe(II) to form siderite and the remainder was lost to the overlying water column. The above mechanism for siderite and magnetite formation also aligns with the presence of *Geospsychobacter* Fe(III)-reducing bacteria and other archaeal Fe(III) reducers in the LSHF mats[29].

Implication for microband formation in BIFs

Role of benthic microbial contribution to Fe-rich microband formation. Our approach provides a detailed modern understanding of interactions between benthic microbial activity, environmental conditions, and Fe-rich minerals where Fe-rich microbands reminiscent of BIFs formed solely in the Y3 mats. It has been suggested that microorganisms played a significant role in the formation of microbands in BIFs[9], a proposition challenged by the low organic C content of <0.8 wt.% in BIFs[1,12,24]. While a mean TOC of ~5 wt.% has been extrapolated from C isotopes, magnetite and siderite mass balance studies of BIF deposits[1], and suggestions made that this organic matter could have been consumed by post-depositional microbial oxidation, direct evidence remains lacking. Our data suggest that microbial-driven siderite and magnetite formation can occur at even much lower organic C content in BIFs. While it is unclear to what extent benthic mats may have contributed to BIF deposition, our observations suggest that the low TOC content in such BIFs, particularly Algoma-type BIFs, may be explained by

Table 2 | Carbon and nitrogen data

Site	Sample ID	Year	Dive	Depth (mbsl)	$\delta^{13}C_{carb}$ (‰, VPDB)	$\delta^{13}C_{org}$ (‰, VPDB)	$\delta^{15}N$ (‰, air)	TOC (wt.%)	TN (wt.%)	Siderite§
South Isabel	M21-SI bulk	2021	1998-10	1699	-5.0	-21.8	3.1	0.32	0.03	No
N37° 17.336 W32° 16.628										
Lava Lake	M23-LL bulk	2023	844-6	1738	-1.2	-25.2	n.d.	0.43	0.02	No
N37° 17.543 W32° 16.796										
Capelinhos	M22-CAP_C bulk	2022	2035-8	1669	-0.3	-24.6	n.d.	0.56	0.04	No
N37° 17.368 W32° 15.834	M23-CAP-sample 1 (upper or bottom part)#	2023	844-6	1669	1.7	-26.7	n.d.	0.83	0.07	n.d.
	M23-CAP-sample 1 (bottom or upper part)#	2023	844-6	1669	1.2	-22.0	n.d.	0.76	0.06	n.d.
Y3	M22-Y3_A bulk	2022	2034-7	1727	-6.0	-35.1	-1.4	0.22	0.03	Yes
N37° 17.518 W32° 16.663	M22-Y3_B (upper part)	2022	2034-7	1727	11.5	-18.9	2.1	0.38	0.03	Limited
	M22-Y3_B (middle part)	2022	2034-7	1727	5.5	-20.9	n.d.	0.26	0.02	Yes
	M22-Y3_B (bottom part)	2022	2034-7	1727	2.0	-21.4	0.9	0.29	0.02	Yes
N37° 17.509 W32° 16.670	M23-Y3 sample 1	2023	846-8	1727	2.0	-33.8	n.d.	0.18	0.02	n.d
	M23-Y3 sample 2	2023	846-8	1727	10.2	−22.8	1.7	0.44	0.03	n.d

#, no orientation; §, mineralogy obtained by XRD and infrared-based and Mössbauer spectroscopies; n.d., not determined.

three main mechanisms from the perspective of biological Fe cycling (Fig. 8b):

(1) *Zetaproteobacteria* that dominate Fe(II) oxidation in benthic marine ecosystems consistently escape encrustation to the surface of the mats to continue the mat-building process, leaving residual mineralized structures to form the framework on which the mat layers are built. The paucity of C in stalks of mat-forming *Zetaproteobacteria* from the Jan Mayen Vent Fields corroborates our interpretation[35]. Regardless of FeOM lifestyles, the residual organic C could originate from a smooth coating of polysaccharides bound to the stalks during cell growth[51].

(2) The remaining residual organic matter is rapidly oxidized by a consortium of microorganisms, a mechanism supported by genome-resolved metagenomics and metatranscriptomics from the Lōʻihi mats[46]. Besides, Fe(III)-reducing microorganisms usually rely on fermenting microbes to produce low molecular weight organic compounds that can be more readily assimilated[83] (Fig. 8a). Fermenters also produce H_2 to facilitate Fe(III) reduction and oxidation of organic molecules for Fe(III) reducers[84]. These microbial communities tend to form a relatively little biomass compared to the large volume of Fe(III)-oxyhydroxides needed for growth because of the much lower amount of energy extractable from Fe(III)-oxyhydroxides compared to O_2 as the terminal electron acceptor. We note that such processes potentially operated in all BIF types if they were associated with enough organic matter to support the development of a similar microbial consortium.

(3) Finally, as evidenced by Fig. 6, the Fe biomineralized filaments provide a large adsorptive surface area for continuous scavenging of considerable amounts of hydrothermally-derived Fe(II) in the absence of direct microbial biomass, collectively forming organic C-poor Fh precursors to FeOx. The resulting substantial increase in Fe_2O_3/SiO_2 ratios from the filamentous microbial structures to the more crystalline FeOx, together with the unique absence of bulk Si-O-Fe elemental bonds, suggest that the gradual Fh transformation dislodges Si during the initial stage of diagenesis (Fig. 8b), offering new insights into formation mechanisms of Fe-rich/Si-poor microbands in BIFs.

Role of environmental contribution to the formation of Si-rich microbands. The exact timing and depositional mechanism of Si-rich layers in BIFs is uncertain. Si enrichment in Precambrian IFs may have originated through the precipitation of Fe-Si gels before reaching the seafloor and their subsequent dewatering and Si release during diagenesis[1], while metamorphic reactions have been proposed for the BIF meso/macrobands[9]. It has also been suggested that the formation of Si-rich layers in Quaternary BIF analogue rocks[4–6] was a syn-depositional feature and controlled mainly by abiotic processes involving for example, cycles of intense and paused hydrothermal/volcanic venting. It was concluded that their deposition with exquisite alternating Fe and Si bands was enabled by basin restriction from the open ocean, resulting in Si saturation and abiotic precipitation from the water column[5,6]. Other studies infer that biannual temperature cycles resulting in episodic abiotic silica saturation could have caused the prominent micro- to mesoband layering in BIFs[85,86]. Alternatively, Si precipitation could occur at, or immediately below, the sediment-water interface in mats along a saturation front with respect to amorphous silica due to the conductive cooling of the local hydrothermal environment[32,38]. Critical explanations about the timing of silica precipitation could come from Si isotope compositions of Si-rich minerals in mats[1,4,32].

As previously discussed, at LSHF, the Fe-rich mats host Si-containing Fh marked by the absence of amorphous Si mineral phases and Si-rich bands, contrasting with other Fe-Si mat-related deposits worldwide[39,59]. Si concentrations of the diffuse hydrothermal fluids are >2 mM at LSHF (Supplementary Table 6), similar to the concentrations in the global oceans that deposited BIFs but much higher than the 0.07 mM of modern seawater[87]. However, diffuse fluid temperatures of ~50–90 °C likely inhibit massive abiotic Si precipitation in the mats, as suggested by PHREEQC thermodynamic calculations (Supplementary Table 6). It is also probable that rapid diffusive dispersal of dissolved Si to the low Si-containing modern ocean compared to Precambrian times, dilutes aqueous Si, thereby inhibiting seawater saturation with regard to silica minerals and precipitation of Si-rich bands. We, therefore, hypothesize that the subseafloor architecture beneath hydrothermal fields, which controls the fluid flow temperature toward the surface, is critical to facilitating abiotic silica precipitation and formation of Si-rich microbands in modern mats during the initial stage of diagenesis. Finally, we suggest that early diagenetic Si-rich microbands would have formed in parallel with the seawater Si precipitation responsible for BIF meso/macrobands.

Contribution of benthic mats to Algoma-type BIFs. We pose the question of whether Fe-metabolizing bacteria as part of microbial mats

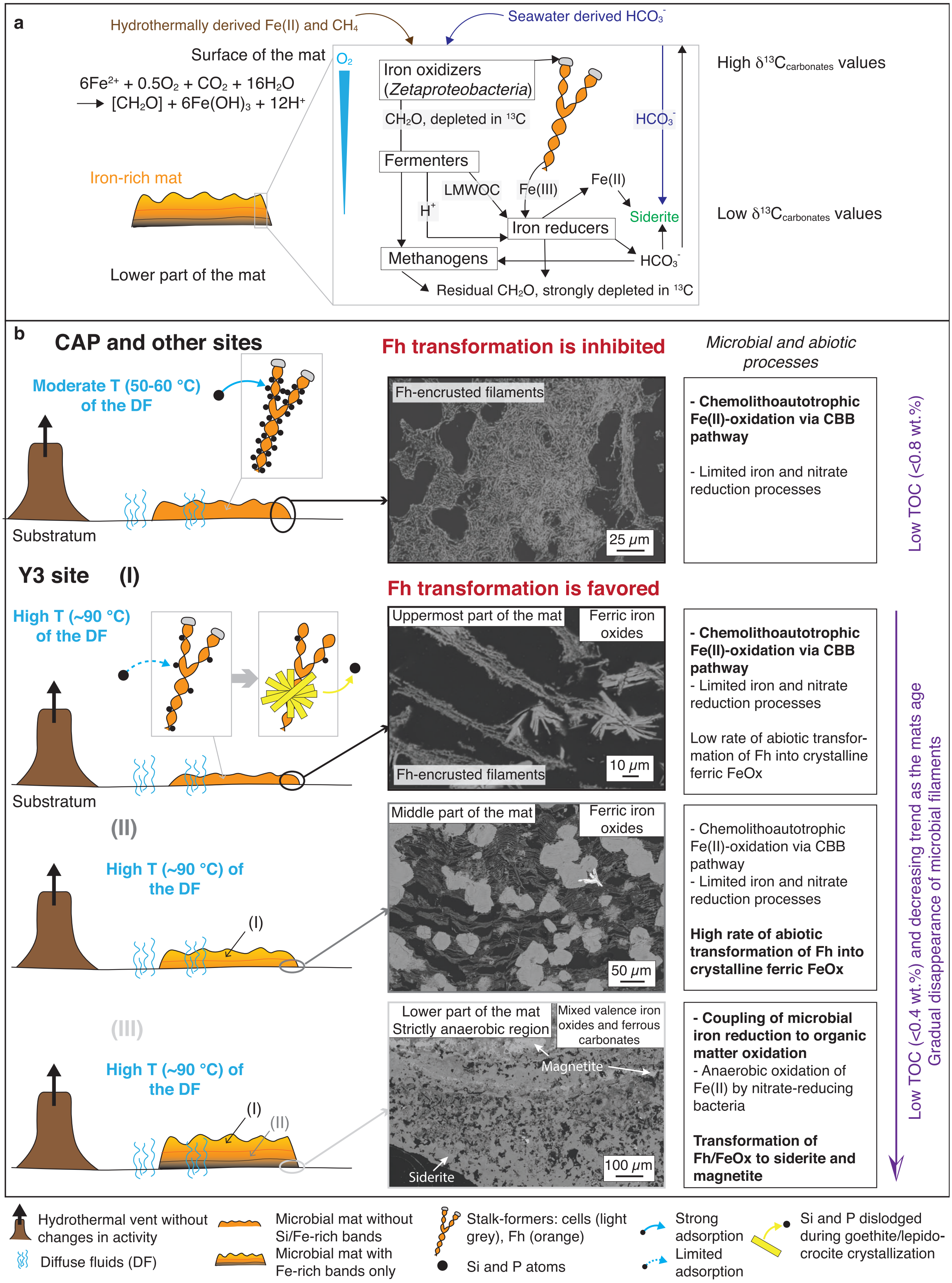

Fig. 8 | Proposed conceptual models of the microbial composition and evolution of the LSHF mats. a Mat trophic structure (Y3 site) and their effect on C isotope compositions. **b** Formation of the Fe-rich microbanding patterns and their related mineralogical composition and biotic/abiotic processes in the LSHF Fe-rich mats. (I-III) Successive steps of the generation of the microbands at Y3. Temperature of the diffuse fluids controls Fh particle size, which, in turn, affects surface area reactivity and adsorption capacity for chemical elements. Note that diffuse hydrothermal fluids were not observed during mat collection at WS, SI, and LL sites. For simplicity, stalk-formers are only represented in these mats. Vertical and horizontal scales are not represented. Not all microbial metabolisms described at LSHF[29,41] and seawater are shown. LMWOC, low molecular weight organic compounds.

were associated with the deposition of Algoma-type BIFs. Our observations point to a relatively rapid and progressive disappearance of Fh-based microbial filaments and possible generation of Fe-rich BIF microbands without phototrophic involvement, although carbon from the lysed planktonic phototroph biomass can fuel Fe(III) reducers and methanogens[84]. Furthermore, our model highlights that magnetite crystallization predates haematite formation as the mats aged and that benthic microbial communities may be a key ingredient for (episodic) siderite-/magnetite-rich microbands in BIFs, which does not preclude existing models of magnetite precipitation in Archean BIFs (see Supplementary discussion).

Overall, we hypothesize that the diffusion efficiency of hydrothermal plumes and the relative location of hydrothermal/volcanic centres to suboxic surface waters would have strongly controlled the development of primitive benthic mats because of the FeOM need for microaerobic conditions. In the late Archean-Paleoproterozoic, these environmental conditions were to be expected where the Fe(II)/O_2 chemocline intersected with the shelf [13,88]. Estimations for O_2 concentrations suggest that dissolved [O_2] of <1 µM in late Archean shallow seawater oases would have jumped to 5–30 µM in the surface ocean at the Archean-Proterozoic transition[45,88]. Considering that the [O_2] in the range of 5-20 µM corresponds to the optimum growth of microaerophilic FeOMs, their proliferation was likely plausible after the GOE. By contrast, the growth of modern FeOMs is limited at 1-5 µM [O_2], although cells are still active[61]. Evolving Archean-Proterozoic seawater [O_2] however likely helped shape the pace of FeOM evolution[47], suggesting that the primitive FeOMs could have evolved and flourished in the presence of nanomolar [O_2] and, thus, contributed to the deposition of BIFs near shallower submarine volcanoes and hydrothermal vent fields to form Algoma-type BIFs. Finally, microbanding patterns formed in the LSHF mat material may be comparable to the Fe-rich microbands of the ~2.5 Ga-old Superior-type BIFs[89,90]. It is, thus, conceivable that similar microband-forming processes could have been operating on the continental shelf if microaerobic Fe(II)-oxidizing conditions were rife, coupled with pulsed delivery of Fe(II)-rich deep-sea hydrothermal vent fluids to shelf environments where Superior-type BIFs formed.

Conclusion

We follow multiple lines of petrographic, mineralogical, and isotopic evidence to show that the development of C-poor Fe-rich BIF microbands could have been controlled by benthic mat-forming microbial processes. Our model shows that these processes begin with microbial oxidation of dissolved hydrothermal Fe(II) by *Zetaproteobacteria*, where microbial filaments provide a large surface of extensive nucleation and removal of dissolved Fe(II) from seawater in the presence or absence of microbial cells. This process is then followed by gradual biotic and abiotic transformation of poorly crystalline Fh into crystalline FeOx minerals as mats aged, during which the Fh-encrusted microbial filaments systematically disappear. Particularly, during early diagenesis, the coupling of sequential microbial reduction of Fh/FeOx to the oxidation of residual organic C by dissimilatory Fe(III)-reducing microorganisms leads to the transformation of Fh/FeOx to secondary crystalline siderite and magnetite. It is suggested that this process points to a key mechanism explaining the low organic C content of BIFs and helps to constrain similar isotopic signatures in BIFs as biomarkers. We suggest that these mechanisms may have been essential to the formation of BIF microbands, particularly in deposits formed in submarine hydrothermal vent fields and continental shelf environments where conducive Fe(II)/O_2 gradients developed. We further propose that the striking absence of Si-rich bands at LSHF can be related to the enduring dominance of high temperature ~50-90 °C diffuse fluids and dispersal of Si to the low Si-containing open ocean, which inhibits the supersaturation state required to drive Si band formation. Importantly, the present study sheds new light on the biotic and abiotic mechanisms by which Fe-rich marine rocks with organic C-poor and Fe-rich microbanding form in the modern ocean and helps explain deep-time observations in which biological processes are difficult to reconstruct.

Methods

Sampling and sample preparation

Mat morphology and their location are described in Table 1[48–50]. The Fe-bearing microbial mats were collected from Capelinhos (CAP), North Tour Eiffel (NTE), South Isabel (SI), West Sintra (WS), Y3, and Lava Lake (LL) sites during the annual MoMARSAT EMSO-Azores Observatory maintenance cruises. Two types of microbial mats were sampled, including flocculent mats at WS, SI, and LL and crumbly mats at CAP, NTE, and Y3 sites between 2021 and 2023[48–50]. The flocculent mats were easily disturbed and resuspended during sample collection. In situ sample collection and on-board sample processing were conducted, as previously described[29,41]. A fraction of each Fe-rich mat was milled into a fine powder in agate mortar for whole-rock mineralogical and geochemical analyses. Thin sections of CAP, NTE, and Y3 mats were made using standard polishing procedures at GET laboratory, University of Toulouse (France). Thin sections were investigated under transmitted and reflected lights using an Olympus BX51 microscope combined with a Olympus SC30 microscope camera.

Diffuse hydrothermal fluids sampling and analysis

Diffuse fluids are limited to the first few dozen metres away from the high temperature chimneys. The diffuse hydrothermal fluid samples of CAP, NTE, and Y3 sites were collected during the MoMARSAT cruise in June 2022[42,49]. Prior to fluid sampling using titanium gas-tight syringe with a fennel-like snorkel, the temperature of diffuse hydrothermal fluids was measured in situ using the temperature sensor of the HOV Nautile submersible. The full procedure for diffuse fluid sampling is described in detail in Wheeler et al.[43]. Aboard the research vessel, hydrothermal fluids were extracted from the fluid sampler, filtered with 0.22-µm Millipore filters and processed on board as described in Chavagnac et al.[43,60]. Aliquots were transferred in acid-cleaned HDPE bottles for a first set of analyses, i.e. density (refractometry), dissolved Fe concentrations (photometry), pH, Eh, salinity, total dissolved salts, dissolved H_2S concentrations, and conductivity (electrodes).

Mineralogical analysis

X-ray diffraction analysis of Mn-poor bulk powder was undertaken with a Panalytical Empyrean diffractometer (CoKα radiation) operating at 35 kV and 45 mA. To determine the mineralogy of Fe- and Mn-rich samples, XRD patterns were acquired with a WAXS Panalytical Empyrean diffractometer (MoKα radiation) operating at 60 kV and 40 mA. In the latter case, a small fraction of bulk powders was mounted in a glass capillary tube of 0.5 mm diameter. Analysis of whole-rock powder samples was performed over angular ranges of 6–76° (CoKα) and 2–30° (MoKα) 2θ and a step size of 0.022° 2θ per 1 s at LPCNO, University of Toulouse III. Peak indexing was performed using Bruker Eva software and mineral identification was carried out by comparing XRD patterns with reference data[53,54].

Short wavelength infrared (SWIR) and Fourier transformed infrared (FTIR) spectroscopies were carried out at IC2MP, University of Poitiers (France), to investigate further mineralogy, structure, and bonding of Fe oxides. SWIR reflectance spectra of bulk rock powders were obtained with a ASD TerraSpec 4 Standards-Resfield spectrometer within the 500–2500 nm range. The spectrometer is equipped with a contact probe including a white light source and three detectors (one Si detector for the 350–1000 nm range with 3 nm resolution and two InGaAs detector for the 1000-2500 nm range with 10 nm resolution). An average of 50 scans was measured on each sample. The Indico Pro software was used to collect the SWIR spectra. FTIR spectra were collected in transmission mode using a Nicolet iS50 FTIR spectrometer equipped with an Ever-Glo source, a potassium bromide (KBr) beamsplitter, and a DTGS KBr detector. Prior to FTIR analyses, KBr pellets, consisting of a mixture of 1 mg of sample and 149 mg of KBr, were prepared. The preparation was pressed for 5 min at 8 kbar to produce pellets and dried overnight in an oven at 120 °C to remove adsorbed water. The FTIR spectra were recorded in the 4000 to 400 cm^{-1} region (middle infrared) and acquired from a mean of 100 scans at a resolution of 4 cm^{-1}. The study of stretching and bending vibrations using FTIR spectroscopy is of deep interest for characterizing adsorbed Si onto Fe oxide surface[55,56].

Because it was difficult to detect poorly crystalline ferrihydrite in the presence of crystalline mineral phases by XRD, the SI, NTE, and Y3 microbial mats were investigated by ^{57}Fe Mössbauer spectroscopy at the Charles Gerhardt Institute, University of Montpellier (France) to characterize Fe-bearing minerals, but also the distribution and redox state of Fe. Analyses were carried out on ca. 300 mg of rock powder loaded in a 30-mm diameter plastic holder irradiated by a ^{57}Co source in rhodium metal. The Mössbauer spectra were acquired using a spectrometer in the constant acceleration mode over the velocity range of −4 to 4 mm/s at room temperature (~ 22 °C). The velocity scale was calibrated using an α-Fe foil. The spectrometer was operated using a triangular velocity waveform for transmission geometry. Gamma rays were detected with a NaI scintillation detector (detection limit of 2%). The Mössbauer spectra were fitted by Lorentzian lines to determine the spectral parameters (IS: isomer shift; QS: electric quadrupole splitting; LW: full line width at half maximum; A: relative resonance areas).

The thin sections were carbon-coated and imaged in BSE mode with a Tescan Vega 4 LMU scanning electron microscope (SEM) equipped with an energy dispersive spectroscopy (EDS) system at GET laboratory. Detailed observations of filamentous structures were conducted on platinum-coated thin sections using a JEOL JSM-6700F field emission SEM at Centre Castaing, University of Toulouse. The SEM-EDS analyses were run at a 10-30 kV accelerating voltage and working distances of 7.9 and 14.7 mm.

Bulk elemental analysis

Whole-rock geochemical analyses of major and trace elements were performed at the clean lab of the GET laboratory. Approximatly 100 mg of bulk rock powders were dissolved using double-distilled reagent acids in closed screw-top Teflon vessels (Savillex). First, samples were digested with a concentrated HNO_3-HCl mixture using a MARS 6 microwave digestion system at 180 °C for 15 min. After evaporation of the solution to dryness on hot plate at 70 °C, samples were dissolved in suprapur HF at 70 °C for 2 h to break down silicates. Major (except Si due to the evaporation of Si-F complexes) and trace elements were measured by ICP-MS using a Thermo Scientific iCAP triple quadrupole instrument, with a precision better than 2%. Calibrations were made with multielemental solutions diluted to different concentrations. The reference material CRPG Mica-Fe was used as a control.

Furthermore, the Si concentration of bulk rock samples were determined by X-Ray Fluorescence (XRF) on glass fusion discs using a PANalytical AXIOS Max spectrometer equipped with an SST-max X-ray tube at RRXG platform, University of Montpellier. The glass fusion discs were prepared by mixing 0.6 g of rock powder with 6 g of lithium tetraborate. We analysed 9 reference geological standards for internal calibration and one external reference standard (IF-G). Loss of ignition (LOI) was determined by heating the rock powders in a muffle furnace at 900 °C for 4 h.

Electron probe micro-analyser

Electron probe micro-analyses (EPMA) were carried out on carbon-coated thin sections using a CAMECA SXFive electron microprobe equipped with five wavelength dispersive spectrometers at Centre Castaing, University of Toulouse III. Analytical conditions of EPMA were performed using a ~1 μm focused beam at 15 kV and 20 nA. The counting time was set to 10 s for all elements. Si, P, and Fe were measured with a focused electron beam and step size of 0.5 μm during quantitative mapping. For silicate EPMA, the instrument was calibrated using reference material standards, including albite for Na, MgO for Mg, Al_2O_3 for Al, wollastonite for Si and Ca, graftonite for P, sanidine for K, Cr_2O_3 for Cr, $MnTiO_3$ for Mn and Ti, haematite for Fe, and $SrSO_4$ for S. For sulfur EPMA, we used the following standards: chalcopyrite for S, Fe, and Cu, mispickel for As, and native Mo for Mo.

Stable isotope analysis

Representative microbial mat samples were analysed for their C isotope ratios of carbonates ($\delta^{13}C_{carb}$) and organic matter ($\delta^{13}C_{org}$) and for their N isotope compositions ($\delta^{15}N$) at Cardiff University. The $\delta^{13}C_{carb}$ analysis was conducted on a Thermo Delta V Advantage mass spectrometer, coupled to a Thermo gasbench II for head-space sampling of carbonate samples. The powdered samples were first weighed into septum vials, which were flushed with helium and then acidified manually with 99% orthophosphoric acid. Samples were then left to react for 24 h at 60 °C to ensure complete reaction of dolomite and siderite. The precision of an in-house Carrara marble standard calibrated against NBS19, expressed as the standard deviation of repeated analyses, resulted in a value 0.07‰ for $\delta^{13}C_{carb}$. For total organic content (TOC), total N (TN), associated $\delta^{13}C_{org}$ and $\delta^{15}N$ compositions, powdered samples acidified in 25% HCl were left to react for two days to eliminate inorganic C. Residues were rinsed three times with ultrapure deionize water to remove remaining acid, dried and weighed into tin capsules. Samples were then measured on a Thermo Delta V Advantage mass spectrometer with Thermo Flash EA and Conflo III. Samples were analysed in combination with three in-house standards composed of a lab-grade caffeine with $\delta^{13}C = -33.30‰$ and two commercial collagen food supplements (MarCol) with a $\delta^{13}C$ of -16.20‰ and an MCF with a $\delta^{13}C$ value of -22.36‰. The in-house standards were calibrated against the international standards IAEA-CH6 and IAEA-600. Data precision, expressed as the standard deviation for repeated analyses of the independent standard MCF, was 0.2‰ (1 SD) for $\delta^{13}C_{org}$ and 0.1‰ (1 SD) for $\delta^{15}N$. The results are reported in the standard δ-notation in ‰ on the Vienna-Pee Dee Belemnite (VPDB) scale for C and air for N.

PHREEQC geochemical modelling

Thermodynamic calculation of the amorphous silica solubility as a function of temperature was performed with the batch reaction option of PHREEQC software package developed by USGS[91]. In addition, the effect of pH was considered and modelled. The calculation of the maximum concentration of dissolved Si required to reach thermodynamic equilibrium between amorphous silica and a standard seawater solution[92] was calculated using the llnl.dat data base[93]. Temperatures were set between 25 °C and 90 °C to represent environmental temperature bathing the microbial mats and the effect of salinity on activity coefficients was taken into account. According to the thermodynamic calculation, the main factor controlling the solubility of Si is temperature rather than pH.

Authors contributions

J.A., E.C.F., and V.C. designed the study. V.C., C.R., C.D., and A.C. collected the samples and, analysed diffuse hydrothermal fluids. J.A., T.D., and F.B. conducted mineralogical analyses. F.P., M.H, A.N., conducted geochemical analyses. C.D. performed PHREEQC modelling. C.R. and V.C. carried out funding acquisition and supervised the project. J.A. drafted the original manuscript and made the figures. The draft was reviewed before submission by E.C.F., C.D., T.D., F.P, F.B, C.R., and V.C.

Data availability

All data are included in present paper and related supplementary information.

Received: 20 September 2024; Accepted: 18 March 2025;

References

1. Konhauser, K.O. et al. Iron formations: A global record of Neoarchaean to Palaeoproterozoic environmental history. *Earth-Sci. Rev.* **172**, 140–177 (2017).
2. Bekker, A. et al. Iron Formations: Their Origins and Implications for Ancient Seawater Chemistry. in *Treatise on Geochemistry* 561–628 (Elsevier). https://doi.org/10.1016/B978-0-08-095975-7.00719-1, (2014).
3. Posth, N.R., Canfield, D.E. & Kappler, A. Biogenic Fe(III) minerals: From formation to diagenesis and preservation in the rock record. *Earth-Sci. Rev.* **135**, 103–121 (2014).

4. Chi Fru, E. et al. Biogenicity of an Early Quaternary iron formation, Milos Island, Greece. *Geobiology* **13**, 225–244 (2015).
5. Chi Fru, E. et al. Sedimentary mechanisms of a modern banded iron formation on Milos Island, Greece. *Solid Earth* **9**, 573–598 (2018).
6. Chi Fru, E. et al. Fossilized iron bacteria reveal a pathway to the biological origin of banded iron formation. *Nat. Commun.* **4**, (2013). 2050.
7. Callac, N. et al. Modes of carbon fixation in an arsenic and CO2-rich shallow hydrothermal ecosystem. *Sci. Rep.* **7**, (2017). 14708.
8. Beukes, N. J. & Gutzmer, J. Origin and Paleoenvironmental Significance of Major Iron Formations at the Archean-Paleoproterozoic Boundary. in *Banded Iron Formation-Related High-Grade Iron Ore* (eds. Hagemann, S., Rosière, C. A., Gutzmer, J. & Beukes, N. J.) vol. 15 0 (Society of Economic Geologists, 2008).
9. Katsuta, N. et al. Major element distribution in Archean banded iron formation (BIF): influence of metamorphic differentiation. *J. Metamorph. Geol.* **30**, 457–472 (2012).
10. Field, E.K. et al. Planktonic marine iron oxidizers drive iron mineralization under low-oxygen conditions. *Geobiology* **14**, 499–508 (2016).
11. Crowe, S.A. et al. Photoferrotrophs thrive in an Archean Ocean analogue. *Proc. Natl. Acad. Sci.* **105**, 15938–15943 (2008).
12. Kappler, A., Pasquero, C., Konhauser, K.O. & Newman, D.K. Deposition of banded iron formations by anoxygenic phototrophic Fe(II)-oxidizing bacteria. *Geology* **33**, 865–868 (2005).
13. Chan, C.S., Emerson, D. & Luther, G.W. III The role of microaerophilic Fe-oxidizing micro-organisms in producing banded iron formations. *Geobiology* **14**, 509–528 (2016).
14. Warke, M.R. et al. The Great Oxidation Event preceded a Paleoproterozoic “snowball Earth. *Proc. Natl. Acad. Sci. USA* **117**, 13314–13320 (2020).
15. Hodgskiss, M.S.W. & Sperling, E.A. A prolonged, two-step oxygenation of Earth’s early atmosphere: Support from confidence intervals. *Geology* **50**, 158–162 (2021).
16. Planavsky, N. et al. Iron-oxidizing microbial ecosystems thrived in late Paleoproterozoic redox-stratified oceans. *Earth Planet. Sci. Lett.* **286**, 230–242 (2009).
17. Li, Y.-L., Konhauser, K.O. & Zhai, M. The formation of magnetite in the early Archean oceans. *Earth Planet. Sci. Lett.* **466**, 103–114 (2017).
18. Tosca, N.J., Guggenheim, S. & Pufahl, P.K. An authigenic origin for Precambrian greenalite: Implications for iron formation and the chemistry of ancient seawater. *GSA Bull.* **128**, 511–530 (2016).
19. Dodd, M.S. et al. Abiotic anoxic iron oxidation, formation of Archean banded iron formations, and the oxidation of early Earth. *Earth Planet. Sci. Lett.* **584**, (2022). 117469.
20. Rasmussen, B., Muhling, J.R. & Krapež, B. Greenalite and its role in the genesis of early Precambrian iron formations – A review. *Earth-Sci. Rev.* **217**, 103613 (2021).
21. Muhling, J.R. & Rasmussen, B. Widespread deposition of greenalite to form Banded Iron Formations before the Great Oxidation Event. *Precambrian Res.* **339**, 105619 (2020).
22. Rasmussen, B., Krapež, B. & Muhling, J.R. Seafloor silicification and hardground development during deposition of 2.5 Ga banded iron formations. *Geology* **43**, 235–238 (2015).
23. Halevy, I., Alesker, M., Schuster, E.M., Popovitz-Biro, R. & Feldman, Y. A key role for green rust in the Precambrian oceans and the genesis of iron formations. *Nat. Geosci.* **10**, 135–139 (2017).
24. Heimann, A. et al. Fe, C, and O isotope compositions of banded iron formation carbonates demonstrate a major role for dissimilatory iron reduction in ~2.5 Ga marine environments. *Earth Planet. Sci. Lett.* **294**, 8–18 (2010).
25. Smith, A. J. B. The Iron Formations of Southern Africa. in *Geology of Southwest Gondwana* (eds. Siegesmund, S., Basei, M. A. S., Oyhantçabal, P. & Oriolo, S.) 469–491 (Springer International Publishing, Cham). https://doi.org/10.1007/978-3-319-68920-3_17 (2018).
26. Smith, A. J. B. et al. Life on a Mesoarchean marine shelf – insights from the world’s oldest known granular iron formation. *Sci. Rep.* **10**, 10519 (2020).
27. Kovalick, A. et al. Living in their heyday: iron-oxidizing bacteria bloomed in shallow-marine, subtidal environments at ca. 1.88 Ga. *Geobiology* **22**, e70003 (2024).
28. Früh-Green, G.L. et al. Diversity of magmatism, hydrothermal processes and microbial interactions at mid-ocean ridges. *Nat. Rev. Earth Environ.* **3**, 852–871 (2022).
29. Astorch-Cardona, A. et al. Linking Zetaproteobacterial diversity and substratum type in iron-rich microbial mats from the Lucky Strike hydrothermal field (EMSO-Azores observatory). *Appl. Environ. Microbiol.* **0**, e02041–23 (2024).
30. Crépeau, V. et al. Diversity and function in microbial mats from the Lucky Strike hydrothermal vent field. *FEMS Microbiol. Ecol.* **76**, 524–540 (2011).
31. Dekov, V. M. et al. Fe–Si-oxyhydroxide deposits at a slow-spreading centre with thickened oceanic crust: The Lilliput hydrothermal field (9°33′S, Mid-Atlantic Ridge). *Chem. Geol.* **278**, 186–200 (2010).
32. Dong, A. et al. Insights from modern diffuse-flow hydrothermal systems into the origin of post-GOE deep-water Fe-Si precipitates. *Geochim. et. Cosmochim. Acta* **317**, 1–17 (2022).
33. Gini, C., et al. Iron Oxyhydroxide-rich hydrothermal deposits at the high-temperature Fåvne Vent Field, Mohns Ridge. *Geochem., Geophys. Geosyst.* **25**, e2024GC011481 (2024).
34. Li, J., et al. Geochemical and Sr-Nd-Pb-Fe Isotopic Constraints on the Formation of Fe-Si Oxyhydroxide Deposits at the Ultraslow-Spreading Southwest Indian Ridge. *Geochem, Geophys. Geosyst.* **25**, e2023GC011185 (2024).
35. Johannessen, K.C., McLoughlin, N., Vullum, P.E. & Thorseth, I.H. On the biogenicity of Fe-oxyhydroxide filaments in silicified low-temperature hydrothermal deposits: Implications for the identification of Fe-oxidizing bacteria in the rock record. *Geobiology* **18**, 31–53 (2020).
36. Kato, S. et al. Iron-based microbial ecosystem on and below the seafloor: a case study of hydrothermal fields of the Southern Mariana Trough. *Front. Microbiol*. **3**, 89 (2012).
37. Li, J., Peng, X., Zhou, H., Li, J. & Sun, Z. Molecular evidence for microorganisms participating in Fe, Mn, and S biogeochemical cycling in two low-temperature hydrothermal fields at the Southwest Indian Ridge. *J. Geophys. Res.: Biogeosci.* **118**, 665–679 (2013).
38. Sun, Z. et al. Generation of hydrothermal Fe-Si oxyhydroxide deposit on the Southwest Indian Ridge and its implication for the origin of ancient banded iron formations. *J. Geophys. Res.: Biogeosci.* **120**, 187–203 (2015).
39. Ta, K., Wu, Z., Peng, X., Luan, Z. & Chen, S. Formation and origin of Fe–Si oxyhydroxide deposits at the ultra-slow spreading Southwest Indian Ridge. *Deep Sea Res. Part I: Oceanogr. Res. Pap.* **170**, 103491 (2021).
40. Langmuir, C. et al. Hydrothermal vents near a mantle hot spot: the Lucky Strike vent field at 37°N on the Mid-Atlantic Ridge. *Earth Planet. Sci. Lett.* **148**, 69–91 (1997).
41. Astorch-Cardona, A., Guerre, M., Dolla, A., Chavagnac, V. & Rommevaux, C. Spatial comparison and temporal evolution of two marine iron-rich microbial mats from the Lucky Strike Hydrothermal Field, related to environmental variations. *Front. Marine Sci.* **10**, 1038192 (2023).
42. Chavagnac, V., Destrigneville, C., Castillo, A. & Hodel, F. Geochemistry of hydrothermal fluids at the Lucky Strike Hydrothermal Field data from the EMSO-Azores observatory. *SEANOE* https://doi.org/10.17882/93162 (2023).
43. Wheeler, B., Cannat, M., Chavagnac, V. & Fontaine, F. Diffuse Venting and Near Seafloor Hydrothermal Circulation at the Lucky Strike Vent

Field, Mid-Atlantic Ridge. *Geochem., Geophys. Geosyst.*25, e2023GC011099 (2024).
44. Anbar, A.D. Elements and Evolution. *Science* **322**, 1481–1483 (2008).
45. Lyons, T. W. et al. Co-evolution of early Earth environments and microbial life. *Nat. Rev Microbiol.* 1–15 https://doi.org/10.1038/s41579-024-01044-y (2024).
46. McAllister, S.M., Vandzura, R., Keffer, J.L., Polson, S.W. & Chan, C.S. Aerobic and anaerobic iron oxidizers together drive denitrification and carbon cycling at marine iron-rich hydrothermal vents. *ISME J.* **15**, 1271–1286 (2021).
47. Ilbert, M. & Bonnefoy, V. Insight into the evolution of the iron oxidation pathways. *Biochim. et. Biophys. Acta ((BBA)) - Bioenerg.* **1827**, 161–175 (2013).
48. Matabos, M. & Sarrazin, J. MOMARSAT2021 cruise, RV L'Atalante. https://doi.org/10.17600/18001296 (2021).
49. Sarradin, P.-M. & Matabos, M. MOMARSAT2022 cruise, RV Pourquoi pas? https://doi.org/10.17600/18001914 (2022).
50. Matabos, M. MOMARSAT2023 cruise, RV L'Atalante. https://doi.org/10.17600/18002419 (2023).
51. Chan, C.S., Fakra, S.C., Emerson, D., Fleming, E.J. & Edwards, K.J. Lithotrophic iron-oxidizing bacteria produce organic stalks to control mineral growth: implications for biosignature formation. *ISME J.* **5**, 717–727 (2011).
52. Chan, C. S. et al. The architecture of iron microbial mats reflects the adaptation of chemolithotrophic iron oxidation in freshwater and marine environments. *Front. Microbiol.* **7**, 796 (2016).
53. Bigham, J. M., Fitzpatrick, R. W. & Schulze, D. G. Iron Oxides. in *Soil Mineralogy with Environmental Applications* (eds. Dixon, J. B. & Schulze, D. G.) 323–366 (John Wiley & Sons, Ltd, Madison). https://doi.org/10.2136/sssabookser7.c10 (2002).
54. Schwertmann, U. & Cornell, R. M. *Iron Oxides in the Laboratory: Preparation and Characterization*. (John Wiley & Sons, 1991).
55. Vempati, R.K. & Loeppert, R.H. Influence of Structural and Adsorbed Si on the Transformation of Synthetic Ferrihydrite. *Clays Clay Min.* **37**, 273–279 (1989).
56. Russell, J. D. & Fraser, A. R. Infrared methods. in *Clay Mineralogy: Spectroscopic and Chemical Determinative Methods* (ed. Wilson, M. J.) 11–67 (Springer Netherlands, Dordrecht). https://doi.org/10.1007/978-94-011-0727-3_2 (1994).
57. Chan, C.S. et al. Microbial Polysaccharides Template Assembly of Nanocrystal Fibers. *Science* **303**, 1656–1658 (2004).
58. Li, J. et al. Elucidating the biomineralization of low-temperature hydrothermal precipitates with varying Fe, Si contents: Indication from ultrastructure and microbiological analyses. *Deep Sea Res. Part I: Oceanogr. Res. Pap.* **157**, 103208 (2020).
59. Sun, Z. et al. Mineralogical characterization and formation of Fe-Si oxyhydroxide deposits from modern seafloor hydrothermal vents. *Am. Mineral.* **98**, 85–97 (2013).
60. Chavagnac, V. et al. Spatial Variations in Vent Chemistry at the Lucky Strike Hydrothermal Field, Mid-Atlantic Ridge (37°N): Updates for Subseafloor Flow Geometry From the Newly Discovered Capelinhos Vent. *Geochem. Geophys. Geosyst.* **19**, 4444–4458 (2018).
61. Maisch, M. et al. Contribution of Microaerophilic Iron(II)-Oxidizers to Iron(III) Mineral Formation. *Environ. Sci. Technol.* **53**, 8197–8204 (2019).
62. McAllister, S.M. et al. The Fe(II)-oxidizing Zetaproteobacteria: historical, ecological and genomic perspectives. *FEMS Microbiol. Ecol.* **95**, fiz015 (2019).
63. Emerson, D., Fleming, E.J. & McBeth, J.M. Iron-oxidizing bacteria: an environmental and genomic perspective. *Annu. Rev. Microbiol.* **64**, 561–583 (2010).
64. Field, E.K. et al. Genomic insights into the uncultivated marine Zetaproteobacteria at Loihi Seamount. *ISME J.* **9**, 857–870 (2015).
65. Konhauser, K.O. et al. Could bacteria have formed the Precambrian banded iron formations?. *Geology* **30**, 1079–1082 (2002).
66. Berg, I.A. et al. Autotrophic carbon fixation in archaea. *Nat. Rev. Microbiol.* **8**, 447–460 (2010).
67. McNevin, D.B. et al. Differences in carbon isotope discrimination of three variants of D-ribulose-1,5-bisphosphate carboxylase/oxygenase reflect differences in their catalytic mechanisms. *J. Biol. Chem.* **282**, 36068–36076 (2007).
68. Bennett, S.A., Hansman, R.L., Sessions, A.L., Nakamura, K. & Edwards, K.J. Tracing iron-fueled microbial carbon production within the hydrothermal plume at the Loihi seamount. *Geochim. et. Cosmochim. Acta* **75**, 5526–5539 (2011).
69. Shanks, W.C. III. Stable Isotopes in Seafloor Hydrothermal Systems: Vent fluids, hydrothermal deposits, hydrothermal alteration, and microbial processes. *Rev. Mineral. Geochem.* **43**, 469–525 (2001).
70. Barker, J.F. & Fritz, P. Carbon isotope fractionation during microbial methane oxidation. *Nature* **293**, 289–291 (1981).
71. Zeng, Z. & Tice, M.M. Promotion and nucleation of carbonate precipitation during microbial iron reduction. *Geobiology* **12**, 362–371 (2014).
72. Johannessen, K.C. et al. Environmental controls on biomineralization and Fe-mound formation in a low-temperature hydrothermal system at the Jan Mayen Vent Fields. *Geochim. et. Cosmochim. Acta* **202**, 101–123 (2017).
73. Toner, B. et al. Mineralogy of iron microbial mats from Loihi Seamount. *Front. Microbiol.* **3**, 118 (2012).
74. Boland, D.D., Collins, R.N., Miller, C.J., Glover, C.J. & Waite, T.D. Effect of solution and solid-phase conditions on the Fe(II)-accelerated transformation of Ferrihydrite to Lepidocrocite and Goethite. *Environ. Sci. Technol.* **48**, 5477–5485 (2014).
75. Hansel, C.M., Benner, S.G. & Fendorf, S. Competing Fe(II)-induced mineralization pathways of ferrihydrite. *Environ. Sci. Technol.* **39**, 7147–7153 (2005).
76. Liu, C. et al. Fe(II)-induced phase transformation of ferrihydrite: The inhibition effects and stabilization of divalent metal cations. *Chem. Geol.* **444**, 110–119 (2016).
77. Hiemstra, T. Ferrihydrite interaction with silicate and competing oxyanions: Geometry and Hydrogen bonding of surface species. *Geochim. et. Cosmochim. Acta* **238**, 453–476 (2018).
78. Hiemstra, T., C. Mendez, J. & Li, J. Evolution of the reactive surface area of ferrihydrite: time, pH, and temperature dependency of growth by Ostwald ripening. *Environ. Sci.: Nano* **6**, 820–833 (2019).
79. Wang, X. et al. Effect of ferrihydrite crystallite size on phosphate adsorption reactivity. *Environ. Sci. Technol.* **47**, 10322–10331 (2013).
80. Das, S., Hendry, M.J. & Essilfie-Dughan, J. Transformation of Two-Line Ferrihydrite to Goethite and Hematite as a Function of pH and Temperature. *Environ. Sci. Technol.* **45**, 268–275 (2011).
81. Bau, M. & Dulski, P. Comparing yttrium and rare earths in hydrothermal fluids from the Mid-Atlantic Ridge: implications for Y and REE behaviour during near-vent mixing and for the Y/Ho ratio of Proterozoic seawater. *Chem. Geol.* **155**, 77–90 (1999).
82. Dymek, R.F. & Klein, C. Chemistry, petrology and origin of banded iron-formation lithologies from the 3800 MA isua supracrustal belt, West Greenland. *Precambrian Res.* **39**, 247–302 (1988).
83. Rico, K.I. et al. Resolving the fate of trace metals during microbial remineralization of phytoplankton biomass in precursor banded iron formation sediments. *Earth Planet. Sci. Lett.* **607**, 118068 (2023).
84. Konhauser, K.O., Newman, D.K. & Kappler, A. The potential significance of microbial Fe(III) reduction during deposition of Precambrian banded iron formations. *Geobiology* **3**, 167–177 (2005).
85. Posth, N.R., Hegler, F., Konhauser, K.O. & Kappler, A. Alternating Si and Fe deposition caused by temperature fluctuations in Precambrian oceans. *Nat. Geosci.* **1**, 703–708 (2008).
86. Schad, M., Halama, M., Bishop, B., Konhauser, K.O. & Kappler, A. Temperature fluctuations in the Archean ocean as trigger for varve-like deposition of iron and silica minerals in banded iron formations. *Geochim. et. Cosmochim. Acta* **265**, 386–412 (2019).

87. Tréguer, P. et al. The Silica Balance in the World Ocean: A Reestimate. *Science* **268**, 375–379 (1995).
88. Wang, C. et al. Archean to early Paleoproterozoic iron formations document a transition in iron oxidation mechanisms. *Geochim. et. Cosmochim. Acta* **343**, 286–303 (2023).
89. Pecoits, E. et al. Petrography and geochemistry of the Dales Gorge banded iron formation: Paragenetic sequence, source and implications for palaeo-ocean chemistry. *Precambrian Res.* **172**, 163–187 (2009).
90. Haugaard, R., Pecoits, E., Lalonde, S., Rouxel, O. & Konhauser, K. The Joffre banded iron formation, Hamersley Group, Western Australia: Assessing the palaeoenvironment through detailed petrology and chemostratigraphy. *Precambrian Res.* **273**, 12–37 (2016).
91. Parkhurst, D. & Appelo, C. Description of input and examples for PHREEQC version 3: a computer program for speciation, batch-reaction, one-dimensional transport, and inverse geochemical calculations. *US geological survey techniques and methods* **6**, 497 (2013).
92. Millero, F.J., Feistel, R., Wright, D.G. & McDougall, T.J. The composition of Standard Seawater and the definition of the Reference-Composition Salinity Scale. *Deep Sea Res. Part I: Oceanogr Res. Pap.* **55**, 50–72 (2008).
93. Johnson, J.W., Oelkers, E.H. & Helgeson, H.C. SUPCRT92: A software package for calculating the standard molal thermodynamic properties of minerals, gases, aqueous species, and reactions from 1 to 5000 bar and 0 to 1000 °C. *Comput. Geosci.* **18**, 899–947 (1992).

Acknowledgements

The MoMARSAT cruises were mainly funded by the French Oceanographic Fleet (FOF). We acknowledge the captains and crews onboard French research vessels *L'Atalante* and *Pourquoi Pas?* as well as the ROV and HOV team during MoMARSAT 2021–2023 campaigns. This study was financially supported by the National Research Agency (ANR) of France as part of the IRONWOMAN project (ANR-21-CE02-0012). Sampling permissions are given by the Portuguese authorities. They are provided in the technical reports of each MoMARSAT cruise available online on the FOF website. The authors are also grateful to the European Union (ERDF) and Région Nouvelle Aquitaine for providing financial support for the study of infrared-based spectroscopy. For scientific discussion, we thank Romain Guilbaud. We are grateful to Fabienne de Parseval (GET, University of Toulouse – UT) for the preparation of high-quality thin sections. We deeply thank Hadrien Henry (GET, UT) for the generation of EPMA element mapping. In addition, Françoise Maubé (GET, UT), Philippe de Parseval (GET, UT), Stéphane Le Blond Du Plouy (Centre Castaing, UT), Nicolas Ratel-Ramond (LPCNO, UT), Simon Cayez (LPCNO, UT), and Moulay Brahim (RRXG platform, University of Montpellier) are thanked for their technical assistance during analytical works. We thank Bertus Smith and 3 anonymous reviewers for their constructive reviews and valuable feedbacks.

Competing interests

The authors declare no competing interests.

Additional information

Supplementary information The online version contains supplementary material available at https://doi.org/10.1038/s43247-025-02223-2.

Correspondence and requests for materials should be addressed to Jérémie Aubineau.

Peer review information *Communications Earth & Environment* thanks Albertus Smith and the other, anonymous, reviewer(s) for their contribution to the peer review of this work. Primary Handling Editor: Carolina Ortiz Guerrero. A peer review file is available.